



NAVAL POSTGRADUATE SCHOOL

MONTEREY, CALIFORNIA

THESIS

**CHARACTERIZATION OF PARTICLES CREATED BY
LASER-DRIVEN HYDROTHERMAL PROCESSING**

by

Andres Camargo

June 2016

Thesis Advisor:
Co-Advisor:
Second Reader:

Sarath K. Menon
Claudia C. Luhrs
Raymond P. Mariella, Jr.

Approved for public release; distribution is unlimited

THIS PAGE INTENTIONALLY LEFT BLANK

REPORT DOCUMENTATION PAGE			<i>Form Approved OMB No. 0704-0188</i>	
Public reporting burden for this collection of information is estimated to average 1 hour per response, including the time for reviewing instruction, searching existing data sources, gathering and maintaining the data needed, and completing and reviewing the collection of information. Send comments regarding this burden estimate or any other aspect of this collection of information, including suggestions for reducing this burden, to Washington headquarters Services, Directorate for Information Operations and Reports, 1215 Jefferson Davis Highway, Suite 1204, Arlington, VA 22202-4302, and to the Office of Management and Budget, Paperwork Reduction Project (0704-0188) Washington, DC 20503.				
1. AGENCY USE ONLY (Leave blank)	2. REPORT DATE June 2016	3. REPORT TYPE AND DATES COVERED Master's thesis		
4. TITLE AND SUBTITLE CHARACTERIZATION OF PARTICLES CREATED BY LASER-DRIVEN HYDROTHERMAL PROCESSING			5. FUNDING NUMBERS	
6. AUTHOR(S) Andres Camargo				
7. PERFORMING ORGANIZATION NAME(S) AND ADDRESS(ES) Naval Postgraduate School Monterey, CA 93943-5000			8. PERFORMING ORGANIZATION REPORT NUMBER	
9. SPONSORING /MONITORING AGENCY NAME(S) AND ADDRESS(ES) N/A			10. SPONSORING / MONITORING AGENCY REPORT NUMBER	
11. SUPPLEMENTARY NOTES The views expressed in this thesis are those of the author and do not reflect the official policy or position of the Department of Defense or the U.S. Government. IRB Protocol number ____N/A____.				
12a. DISTRIBUTION / AVAILABILITY STATEMENT Approved for public release; distribution is unlimited			12b. DISTRIBUTION CODE	
13. ABSTRACT (maximum 200 words) <p>This study examined particles created by laser-driven hydrothermal processing, an innovative technique used for the ablation of submerged materials. Two naturally occurring materials, obsidian and tektite, were used as targets for this technique. Characterization of sample materials before and after laser processing was conducted through multiple techniques such as optical microscopy, X-ray diffraction, scanning electron microscopy, transmission electron microscopy, and energy dispersive X-ray spectroscopy.</p> <p>Examination of the untreated base material, in bulk and crushed form, established a baseline for comparison to particles created by laser processing of the same material. Characterization methods provided data of micron- and nano-sized particles, including their crystal structure, microstructure, and chemical composition.</p> <p>The bulk and crushed obsidian and tektite samples contained inclusions and particles rich in several transition elements, most notably iron and titanium. Analysis of liquid media collected after laser processing of bulk obsidian and tektite samples revealed fine particles rich in the same elements. Evidence suggests laser-driven hydrothermal processing separates heavy elements from the mostly amorphous silica matrix encountered in the materials examined.</p>				
14. SUBJECT TERMS laser-driven hydrothermal processing, characterization, obsidian, tektite, natural glass			15. NUMBER OF PAGES 89	
			16. PRICE CODE	
17. SECURITY CLASSIFICATION OF REPORT Unclassified	18. SECURITY CLASSIFICATION OF THIS PAGE Unclassified	19. SECURITY CLASSIFICATION OF ABSTRACT Unclassified	20. LIMITATION OF ABSTRACT UU	

THIS PAGE INTENTIONALLY LEFT BLANK

Approved for public release; distribution is unlimited

**CHARACTERIZATION OF PARTICLES CREATED BY LASER-DRIVEN
HYDROTHERMAL PROCESSING**

Andres Camargo
Lieutenant Commander, United States Coast Guard
B.S., United States Merchant Marine Academy, 2002

Submitted in partial fulfillment of the
requirements for the degree of

MASTER OF SCIENCE IN MECHANICAL ENGINEERING

from the

**NAVAL POSTGRADUATE SCHOOL
June 2016**

Approved by: Sarath K. Menon
 Thesis Advisor

Claudia C. Luhrs
Co-Advisor

Raymond P. Mariella, Jr.
Second Reader

Garth V. Hobson
Chair, Department of Mechanical and Aerospace Engineering

THIS PAGE INTENTIONALLY LEFT BLANK

ABSTRACT

This study examined particles created by laser-driven hydrothermal processing, an innovative technique used for the ablation of submerged materials. Two naturally occurring materials, obsidian and tektite, were used as targets for this technique. Characterization of sample materials before and after laser processing was conducted through multiple techniques, such as optical microscopy, X-ray diffraction, scanning electron microscopy, transmission electron microscopy, and energy dispersive X-ray spectroscopy.

Examination of the untreated base material, in bulk and crushed form, established a baseline for comparison to particles created by laser processing of the same material. Characterization methods provided data of micron- and nano-sized particles, including their crystal structure, microstructure, and chemical composition.

The bulk and crushed obsidian and tektite samples contained inclusions and particles rich in several transition elements, most notably iron and titanium. Analysis of liquid media collected after laser processing of bulk obsidian and tektite samples revealed fine particles rich in the same elements. Evidence suggests laser-driven hydrothermal processing separates heavy elements from the mostly amorphous silica matrix encountered in the materials examined.

THIS PAGE INTENTIONALLY LEFT BLANK

TABLE OF CONTENTS

I.	INTRODUCTION.....	1
A.	MOTIVATION	1
B.	BACKGROUND	1
C.	FOCUS OF PRESENT STUDY	4
D.	APPROACH.....	4
II.	EXPERIMENTAL METHODS	7
A.	MATERIALS AND EQUIPMENT	8
1.	Obsidian Samples.....	8
2.	Tektite Samples	8
3.	Sample Preparation For Analysis.....	9
B.	CHARACTERIZATION TECHNIQUES.....	11
1.	Optical Microscopy	11
2.	X-Ray Diffractometry.....	12
3.	Scanning Electron Microscopy	13
4.	Energy Dispersive X-Ray Spectroscopy.....	14
5.	Transmission Electron Microscopy	14
III.	RESULTS AND DISCUSSION	17
A.	BASE MATERIAL CHARACTERIZATION	17
1.	Obsidian	17
2.	Tektite	25
B.	POST-LDHP MATERIAL CHARACTERIZATION.....	34
1.	Obsidian	34
a.	<i>Studies on Sample Surface after LDHP.....</i>	<i>34</i>
b.	<i>Studies on Particles in Deionized Water after LDHP</i>	<i>38</i>
2.	Tektite	46
a.	<i>Studies on Sample Surface after LDHP.....</i>	<i>46</i>
b.	<i>Studies on Particles in Deionized Water after LDHP</i>	<i>50</i>
C.	SUMMARY OF POST-LDHP PARTICLES OBSERVED.....	57
IV.	CONCLUSION	61
V.	FUTURE WORK	65
	LIST OF REFERENCES	67

INITIAL DISTRIBUTION LIST	69
--	-----------

LIST OF FIGURES

Figure 1.	General arrangement of experiment showing the path of laser to sample (left) and closer view of a sample in holder with particle cloud (right). Source: [4].....	2
Figure 2.	Images of quartzite before (left) and after (right) LDHP treatment. Treated sample exposed to 351-nm, 15-ns laser pulses: upper three craters with 7 J/cm ² fluence at 0.5 GW/cm ² intensity and lower four craters with 3.5 J/cm ² at 0.25 GW/cm ² intensity. Adapted from [4].	3
Figure 3.	Image of LDHP removing surface material and suspension of particles in liquid media. Adapted from [4].	3
Figure 4.	Bulk obsidian sample.	8
Figure 5.	Bulk tektite samples.	8
Figure 6.	Buehler ISOMET low speed saw cutting tektite sample.	9
Figure 7.	Buehler SIMPLIMET 2 mounting press (left), PROBEMET conducting compound (center), and ECOMET 4 automatic polisher (right).	10
Figure 8.	Buehler ECOMET 3 automatic polisher.	10
Figure 9.	Buehler VibroMet 2 vibratory polisher (left) and ULTRAMET 2005 sonic cleaner (right).	11
Figure 10.	Nikon EPIPHOT 200 optical microscope.	12
Figure 11.	Rigaku MiniFlex 600 X-ray diffractometer.	13
Figure 12.	Zeiss NEON 40 field emission scanning electron microscope.	13
Figure 13.	Cressington 208HR high resolution sputter coater.	14
Figure 14.	Pelco 2251 vacuum desiccator.	14
Figure 15.	FEI Tecnai Osiris transmission electron microscope.	15
Figure 16.	Optical micrographs of polished sections of bulk obsidian showing inclusions and porosity.	17
Figure 17.	Images of a bulk obsidian sample before (left) and after (right) crushing with a mortar and pestle.	18
Figure 18.	XRD diffraction patterns of bulk (red) and crushed (blue) obsidian samples.	18
Figure 19.	EDS spectrum of bulk obsidian sample.	19
Figure 20.	Secondary electron image of bulk obsidian sample (top). SEM-EDS mapping of same bulk obsidian sample showing Si distribution among the sample (bottom left) and Fe-rich oxide particles randomly	

	distributed throughout the sample (bottom right). Note the large Fe-rich particle on the top left section of the Fe-K map.	20
Figure 21.	Secondary electron image of a crushed obsidian sample (top left). SEM-EDS mapping showing Si distribution (top right), Fe-rich oxide particles (bottom left), and Al-rich oxide particles (bottom right).....	21
Figure 22.	Secondary electron image of a crushed obsidian sample showing Fe-rich and Al-rich oxide particles circled in red.	22
Figure 23.	SEM-EDS spectra of a Fe-rich oxide particle (left) and Al-rich oxide particle (right).	23
Figure 24.	BF-STEM (left) and HAADF-STEM (right) images of crushed obsidian sample particles.	24
Figure 25.	STEM-EDS mapping showing oxide particles rich in Si (top right), Ti (bottom left), and Al (bottom right).	24
Figure 26.	STEM-EDS mapping showing oxide particles rich in Si (bottom left) and Fe (bottom right).	25
Figure 27.	Optical Micrographs of Polished Sections of Bulk Tektite Samples showing Porosity.....	25
Figure 28.	Images of a bulk tektite sample before (left) and after (right) crushing with a mortar and pestle.	26
Figure 29.	XRD diffraction patterns of bulk (green) and crushed (orange) tektite samples.....	27
Figure 30.	XRD diffraction pattern of bulk tektite sample with 70% crystallinity.	27
Figure 31.	EDS Spectrum of Bulk Tektite Sample.	29
Figure 32.	Secondary electron images showing porosity in the surface of a polished bulk tektite sample.....	30
Figure 33.	Secondary Electron image of a crushed tektite sample (top left). SEM-EDS mapping showing Si distribution (top right), Fe-rich oxide particle (bottom left), and Al-rich oxide particles (bottom right).....	30
Figure 34.	Secondary electron images showing (a) area of crushed tektite and (b) crushed tektite particle analyzed. Red box indicates particle analyzed for Table 4 and Figure 35.	31
Figure 35.	SEM-EDS spectra of (a) crushed tektite area and (b) crushed tektite particle corresponding to Figure 32.	32
Figure 36.	BF-STEM (left) and HAADF-STEM (right) images of crushed tektite particles. Scale bar 500 nm.	33

Figure 37.	STEM-EDS mapping showing oxide particles rich in Si (top right), Ti (bottom left), and Al (bottom right).	33
Figure 38.	Post-LDHP obsidian (sample ID B7) showing six areas (red arrows) exposed to 5000, 248-nm laser pulses per crater.	35
Figure 39.	Secondary electron images showing effects of LDHP treatment on the surface of obsidian (sample ID B7). (a) Border of treated area 6. (b) Untreated surface between treated areas 4 and 5. (c) Increased magnification in the center of treated area 5 showing cuts presumably made by laser pulses. (d) Increased magnification of section in (c) showing the appearance of material solidification after melting.	36
Figure 40.	Image of LDHP treatment on surface of obsidian (sample ID B9). Treated area optically white/translucent in color from exposure to 300, 351-nm pulses.	37
Figure 41.	EDS spectra of obsidian sample B9 showing untreated area (left) and LDHP treated area (right).	38
Figure 42.	Image of particles collected from post-LDHP treatment on obsidian sample. Note the optically white/translucent appearance of the particles. Source: [21].	39
Figure 43.	Secondary electron image of post-LDHP obsidian particles collected from sample BC14 (top). SEM-EDS mapping showing Si distribution (bottom left) and Fe-rich oxide particles (bottom right).	40
Figure 44.	Secondary electron images showing two different post-LDHP obsidian particle areas from sample BC14 at x150 magnification (left) and x500 magnification (right). Red boxes indicate particle 1 (left) and particle 2 (right) analyzed for Table 6.	40
Figure 45.	EDS spectra of particle 1 (left) and particle 2 (right) from post-LDHP obsidian particle sample BC14.	41
Figure 46.	BF-STEM (left) and HAADF-STEM (right) images of post-LDHP obsidian particles in sample BC14SN. Scale bar 500 nm.	42
Figure 47.	STEM-EDS mapping of post-LDHP obsidian particles in sample BC14SN showing oxide particles rich in Si (middle left), Ti (middle right), Fe (bottom left) and Al (bottom right).	43
Figure 48.	HRTEM images showing crystallinity in a particle among an amorphous matrix from post-LDHP obsidian particles in sample BC14SN. (a) 80-nm inclusion within post-LDHP obsidian particle. (b) Increased magnification of outer edge of inclusion in (a) showing 18-nm particle. (c) Increased magnification of outer edge of particle in (b) showing lattice planes with average plane spacing determined to be 0.254 nm.	45

Figure 49.	HRTEM image of particle with crystallinity from post-LDHP obsidian in sample BC14SN. Red box indicates area measured to determine chemical compound based on plane spacing.	45
Figure 50.	Post-LDHP tektite showing three areas exposed to 100 (1 and 2) and 200 (3), 1065-nm laser pulses per crater. Source: [22].	47
Figure 51.	Image of crater 3 showing the appearance of crystals in post-LDHP tektite sample. Image captured by a Keyence VHX-5000 optical imaging profilometer at LLNL. Source: [20].	48
Figure 52.	Secondary electron images showing effects of LDHP treatment on the surface of tektite (sample ID 21DEC15 Tektite). Image of border in area 1 showing treated and untreated sections (top left). Image of border in area 2 showing treated and untreated sections (bottom left).	49
Figure 53.	Secondary electron images showing effects of LDHP treatment on the surface of tektite. Treated surface in area 3 (top right). Increased magnification in the center of area 3 showing a hole in the surface and the appearance of material solidification after melting (bottom right).	49
Figure 54.	Secondary electron image of post-LDHP tektite particles collected from deionized water (top). SEM-EDS mapping showing Si-rich oxide particles (middle left), Ti-rich oxide particles (middle right), Fe-rich oxide particles (bottom left) and Al-rich oxide particles (bottom right).	52
Figure 55.	Secondary electron image of post-LDHP tektite particles analyzed showing significantly different chemical compositions. Red boxes indicate particles analyzed.	53
Figure 56.	EDS spectra of particle 1 (top), particle 2 (bottom left) and particle 3 (bottom right) from post-LDHP tektite particle sample.	54
Figure 57.	BF-STEM (left) and HAADF-STEM (right) images of crushed tektite particles. Scale bar 500 nm.	55
Figure 58.	STEM-EDS mapping showing oxide particles rich in Si (middle left), Ti (middle right), Fe (bottom left) and Al (bottom right).	56
Figure 59.	Diagram of possible mechanism of LDHP.	59

LIST OF TABLES

Table 1.	Summary of material samples.....	7
Table 2.	Chemical composition of bulk obsidian sample and rhyolitic obsidian [7].	19
Table 3.	Chemical composition of Fe-rich and Al-rich oxide particles from Figure 22.	22
Table 4.	Chemical composition of bulk tektite sample and tektite sample J71 Sangiran Java [19].....	28
Table 5.	Chemical Composition Comparison between Bulk Tektite, Crushed Tektite Area, and Crushed Tektite Particle.	31
Table 6.	Comparison of chemical composition between untreated and LDHP treated areas of obsidian sample B9.....	37
Table 7.	Comparison of chemical composition between bulk obsidian sample, post-LDHP particle 1, and post-LDHP particle 2.	41
Table 8.	Comparison of chemical composition between bulk tektite sample, average of post-LDHP untreated areas, crater 1, crater 2 and crater 3.	50
Table 9.	Comparison of chemical composition between bulk tektite sample, post-LDHP particle 1, post-LDHP particle 2 and post-LDHP particle 3.....	53
Table 10.	Summary of post-LDHP particles observed.	58

THIS PAGE INTENTIONALLY LEFT BLANK

LIST OF ACRONYMS AND ABBREVIATIONS

Al	aluminum
at%	atomic percent
BF-STEM	bright field scanning transmission electron microscopy
Cu	copper
DI	deionized water
EDS	energy dispersive X-ray spectroscopy
Fe	iron
HAADF-STEM	high-angle angular dark field scanning transmission electron microscopy
ICDD	International Center for Diffraction Data
lb	pound
KV	kilovolt
LDHP	laser-driven hydrothermal processing
LLNL	Lawrence Livermore National Laboratory
mA	milliamp
Mg	magnesium
min	minute
N	Newton
Nd:YAG	neodymium-doped yttrium aluminum garnet
Nd:YLF	neodymium-doped yttrium lithium fluoride
Nd:YLF&APG1	neodymium-doped yttrium lithium fluoride and aluminum-phosphate glass-1
nm	nanometer
rpm	revolution per minute
SEM	scanning electron microscope
Si	silicon
SiC	silicon carbide
TEM	transmission electron microscope
Ti	Titanium
wt%	weight percent

XRD

X-ray diffractometer

μm

micrometer

ACKNOWLEDGMENTS

I would like to thank my thesis advisors, Professors Sarath Menon and Claudia Luhrs, for their exceptional guidance and support throughout my coursework and research. I would also like to thank Dr. Ray Mariella Jr. at Lawrence Livermore National Laboratory for welcoming me to be a part of this project and for the invaluable insight into his work. Without them, this thesis would not have been possible.

Thank you to the U.S. Coast Guard for selecting me for this opportunity to achieve a higher education. I hope to use the knowledge and experience gained at the Naval Postgraduate School to help enhance the fleet.

Finally, and most importantly, I dedicate this work to my wife, Shawn, and our three children, Sebastian, Alyssandra, and Gabriel. Their love and support enabled me to pursue and achieve what I thought would not have been possible.

THIS PAGE INTENTIONALLY LEFT BLANK

I. INTRODUCTION

A. MOTIVATION

Nuclear forensics is the analysis of nuclear or radioactive materials to gather evidence and determine the original source [1]. Nuclear or radioactive material can come from a seized nuclear weapon or from debris following a nuclear event. Central to nuclear forensics, investigators rely on physical, chemical, and/or isotopic analysis of these materials to piece together relevant data [2], [3]. This helps investigators determine where the materials originated from and develop a relationship between the material characteristics and its process history [1].

Analysis methods require techniques that collect the material without contamination while ensuring no loss of sample material [4]. A particular method of collecting material for analysis includes the comminution of refractory materials through a novel technique termed laser-driven hydrothermal processing developed by Dr. Raymond P. Mariella Jr., Senior Scientist, at Lawrence Livermore National Laboratory (LLNL) in Livermore, CA. This technique enables the user to rapidly comminute material without contamination, while being environmentally safe and field deployable [5]. This method may be applied primarily by U.S. nuclear-related agencies, potentially with U.S. Department of Homeland Security and Department of Defense partners. Civilian agencies and industry can find this technique especially useful for conventional methods of chemical analysis of a material when small quantities are available. There is an issued patent and pending patent application for use of the technology for other applications such as decontamination of building and structures of nuclear facilities, especially during decommissioning or nuclear-related accident [6], [7]. Additionally, this technique has been shown to be implemented remotely with a robotic system avoiding the risk of exposure to personnel [8].

B. BACKGROUND

Laser-driven hydrothermal processing (LDHP) is an innovative technology developed to comminute material in a submerged environment. Using a neodymium-doped

yttrium lithium fluoride (Nd:YLF) slab laser in a 2013 study [4], LDHP was used in the 30 MW/cm² and 500 MW/cm² intensity range using 15-ns, 351-nm laser pulses with an energy range of 1 J to 0.35 J to strike impure, non-metallic materials (quartzite and concrete) submerged in water. Mariella et al. [4] observed that at these conditions, LDHP dissolved or converted material from a solid substrate into ultrafine particles in a controlled method. Ablation of solid substrates was also studied at LDHP parameters below 100 MW/cm² intensity and 0.4 J/cm² fluence. Figure 1 is an image of the arrangement of an experiment showing the path of the laser through the liquid to strike the sample surface.

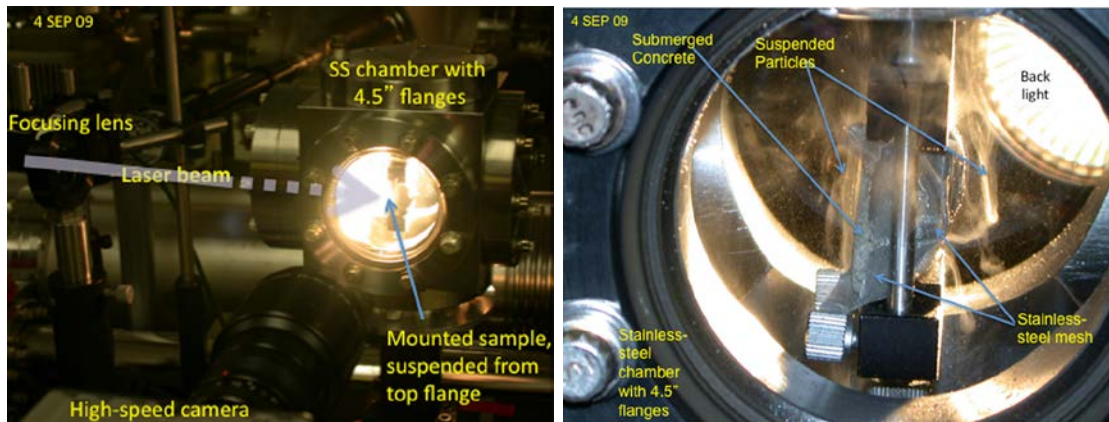


Figure 1. General arrangement of experiment showing the path of laser to sample (left) and closer view of a sample in holder with particle cloud (right). Source: [4].

This process appeared to neither cause chemical reactions nor induce boiling or sublimation in tested material. However, analysis of the results of experiments on quartzite (Figure 2) and concrete appeared to support the notion that surface material was transiently dissolved and redeposited onto the surface. In Figure 2, note the seven craters created by LDHP as indicated by the blue arrows.



Figure 2. Images of quartzite before (left) and after (right) LDHP treatment. Treated sample exposed to 351-nm, 15-ns laser pulses: upper three craters with 7 J/cm^2 fluence at 0.5 GW/cm^2 intensity and lower four craters with 3.5 J/cm^2 at 0.25 GW/cm^2 intensity. Adapted from [4].

Data suggested that a thin layer of high-pressure, high-temperature water created by the laser pulses transiently dissolves the material surface. It is thought that when this thin-layer returns to atmospheric pressure and near-ambient temperature, the dissolved material precipitates as suspended particles in the liquid media, or as SiO_2 crystals at the target surface (in the case of the quartzite target) [4]. Figure 3 provides an overview of LDHP on a material composed of SiO_2 .

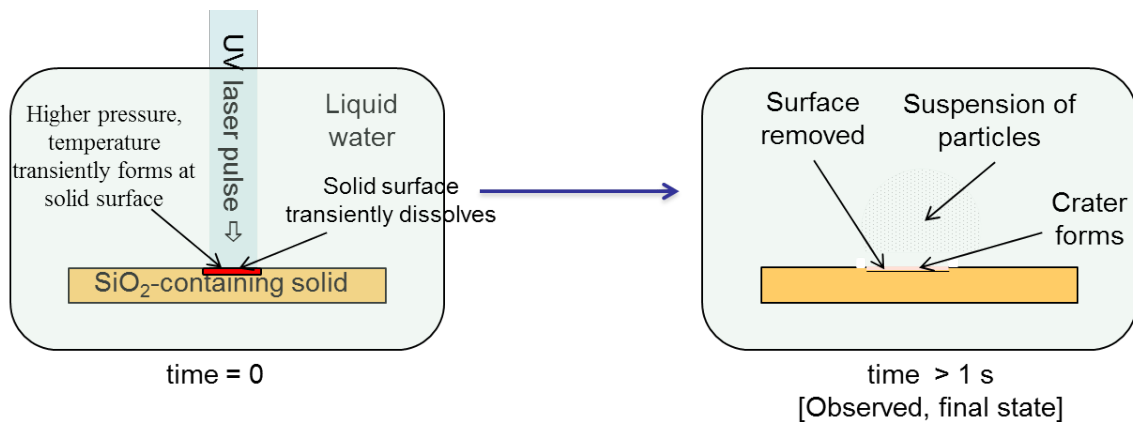


Figure 3. Image of LDHP removing surface material and suspension of particles in liquid media. Adapted from [4].

At the time of the experiments conducted in [4], it was thought that the formation of SiO₂ crystals that surround the surface removed potentially indicated that suspended particles created by LDHP also consisted primarily of SiO₂. Additionally, it was unknown which material elements were transiently and/or permanently dissolved when exposed to LDHP. Therefore, electron microscopy techniques, including EDS analysis, were required to study the suspended particles produced by LDHP and the mechanisms involved.

Two naturally occurring materials, obsidian and tektite, were selected for this study for two reasons: (i) Both materials are compositionally high in SiO₂ and (ii) form similarly to glass formed by a nuclear explosion, which creates massive pressures and temperatures. As an example, trinitite is a glass formed by a post-nuclear event with SiO₂ making up 50%-75% of its chemical composition [3], [9]. Obsidian forms under high pressure and temperature by volcanic activity and tektite forms as a result of meteoritic impact on earth's surface, with both being compositionally high in SiO₂ [10]-[12].

C. FOCUS OF PRESENT STUDY

Due to the unknown composition of the suspended particles and mechanisms involved in their creation by LDHP, this study focused on the methodical characterization of these particles and the exposed material surface. Based on experiments from [4], particles produced varied in size from a few microns to less than 50 nm. Therefore, the use of electron microscopy techniques were best suited for analysis. This was the first detailed study of the suspended particles created by LDHP, including the base material and particles found in and around the LDHP treated areas. The results contained herein provided the critical first step in understanding how these particles form and how LDHP comminutes the surface of a material in a liquid environment.

D. APPROACH

Characterization techniques were conducted through optical microscopy, X-ray diffraction (XRD), scanning electron microscopy (SEM), transmission electron microscopy (TEM), and energy dispersive X-ray spectroscopy (EDS) of each material before and after exposure to LDHP treatment while submerged in deionized water. These

techniques determined material and particle morphology, crystal structure, and chemical composition, and what changes, if any, occurred after LDHP.

This approach paved the way for follow on quantitative studies to include particle size analysis to determine particle size distribution, and the role of various LDHP parameters in the creation of particles. The results contained in this study were instrumental towards determining the mechanism of particle formation.

THIS PAGE INTENTIONALLY LEFT BLANK

II. EXPERIMENTAL METHODS

With the core of this study being the characterization the particles created from LDHP the first experimental step was to analyze the base materials to create a baseline to determine if any changes occurred during laser processing. Initially, one obsidian and three tektite bulk samples were received, cut, polished and analyzed. During LDHP, the material removed from the substrate produced fine particles that were collected in the liquid media. The color of the obsidian studied is black and from visual observations made from the particles present in the liquid after LDHP, it was observed that the powder collected was optically white/translucent. As part of this study, a small portion of an obsidian and tektite bulk sample was manually pulverized with a mortar and pestle, and then prepared and analyzed as well. As a result, 10 samples (eight bulk and two crushed) established a baseline before treatment with LDHP. Table 1 summarizes those samples.

Table 1. Summary of material samples.

<i>Mineral</i>	<i>Form</i>	<i>Number of Samples</i>
Obsidian	Bulk	2
	Crushed	1
Tektite	Bulk	6
	Crushed	1

LDHP products were provided from laser processing of one bulk obsidian sample and one tektite sample in deionized water. Representative samples of each LDHP product in deionized water were provided by LLNL. Samples were centrifuged for 15 minutes at 12,500 rpm then 2–3 drops placed on mounted carbon tabs and TEM grids and left overnight to dry.

A. MATERIALS AND EQUIPMENT

1. Obsidian Samples

Obsidian samples (Figure 4) were provided by LLNL. Samples originated from Lake County, OR.



Figure 4. Bulk obsidian sample.

2. Tektite Samples

Tektite samples (Figure 5) were purchased from a commercial source (Mama's Minerals, Albuquerque, NM). Samples originated from Indonesia.



Figure 5. Bulk tektite samples.

3. Sample Preparation for Analysis

Eight samples were cut from the bulk material (two samples from each) to 2 mm thickness. Due to the different sizes and shapes of the bulk material, the length and width varied among each sample with an average dimension of 18.5 mm \times 10.7 mm. Cutting was completed with a Buehler ISOMET low speed saw using a Buehler IsoCut wafering blade (Figure 6) at a speed setting of 7 (200 rpm).



Figure 6. Buehler ISOMET low speed saw cutting tektite sample.

Four samples (one sample from each bulk material) was mounted in a conducting compound using a Buehler SIMPLIMET 2 mounting press with Buehler PROBEMET conductive molding compound (Figure 7). Initial polishing was completed on a Buehler ECOMET 4 automatic polisher (Figure 7) at 120 rpm with a 17.8 N (4 lb) load starting with 320-grit SiC paper with increasing increments of 500-grit, 1200-grit, 2500-grit, and 4000-grit SiC paper at 120 rpm with a 26.7 N (6 lb) load. Initial polishing time at each grit was approximately 20 minutes.



Figure 7. Buehler SIMPLIMET 2 mounting press (left), PROBEMET conducting compound (center), and ECOMET 4 automatic polisher (right).

Next, additional polishing was completed using a Buehler ECOMET 3 automatic polisher (Figure 8) with a Buehler microcloth pad coated by 1 μm alumina suspension. Samples were polished with a 31.1 N (7 lb) load for approximately 60 minutes.



Figure 8. Buehler ECOMET 3 automatic polisher.

Final polishing was conducted on a Buehler VibroMet 2 vibratory polisher (Figure 9). All samples were placed in a 0.05 μm alumina suspension at 80% amplitude

for approximately 24 hours. Samples were then cleaned in a Buehler ULTRAMET 2005 sonic cleaner (Figure 9) in deionized water for approximately 30 minutes.



Figure 9. Buehler VibroMet 2 vibratory polisher (left) and ULTRAMET 2005 sonic cleaner (right).

B. CHARACTERIZATION TECHNIQUES

1. Optical Microscopy

A Nikon EPIPHOT 200 inverted optical microscope (Figure 10) was used to determine the surface structure of each sample. Images of each mounted sample were collected at x25, x100, x200, x500, and x1000 magnification then viewed to analyze morphological details of each specimen.



Figure 10. Nikon EPIPHOT 200 optical microscope.

2. X-Ray Diffractometry

Of the eight samples, part of one bulk obsidian sample and part of one bulk tektite sample were crushed using a mortar and pestle. A Rigaku MiniFlex 600 X-ray diffractometer (Figure 11) was then used to determine crystallinity of all ten samples (eight bulk samples and two crushed samples). XRD measurement conditions were set to scan in the 2θ angle at a range of 10–100 degrees with a 0.02 degree step width and 4 degree/min scan speed. This resulted in the collection of intensity versus 2θ diffraction angle for each sample. Diffraction data was then analyzed using PDXL2 software along with International Center for Diffraction Data (ICDD) crystallographic structure parameter database.



Figure 11. Rigaku MiniFlex 600 X-ray diffractometer.

3. Scanning Electron Microscopy

A Zeiss NEON 40 field emission SEM (Figure 12) was used to determine the morphology of obsidian and tektite bulk, crushed, and LDHP samples.

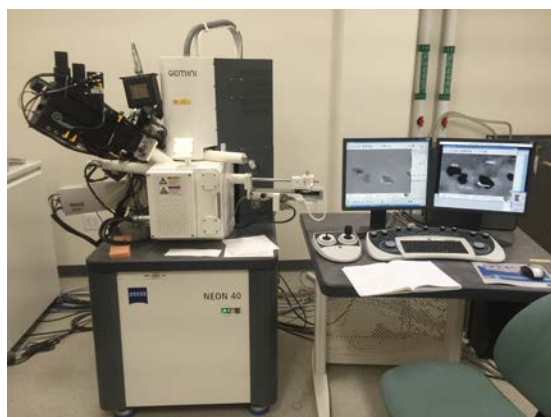


Figure 12. Zeiss NEON 40 field emission scanning electron microscope.

Bulk and crushed samples are electrically non-conducting and hence were coated with a 2-nm layer of Pt-20Pd using a Cressington 208HR high resolution sputter coater (Figure 13) for electron microscopy observations and kept overnight in Pelco 2251 vacuum desiccator (Figure 14) before being placed in the SEM for analysis. Coated samples were observed under 20 KV with a 1.33×10^{-6} mA beam current. LDHP samples were observed under 5 KV with a 0.18×10^{-6} mA beam current.



Figure 13. Cressington 208HR high resolution sputter coater.

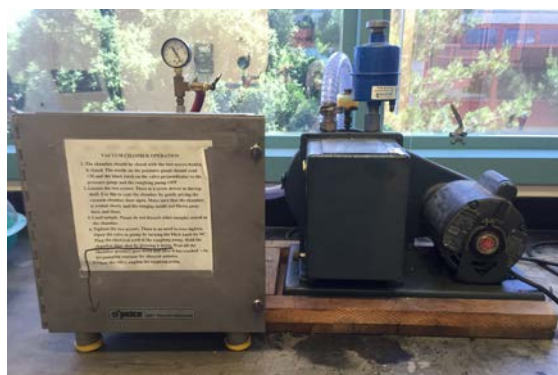


Figure 14. Pelco 2251 vacuum desiccator.

4. Energy Dispersive X-Ray Spectroscopy

EDS analysis was conducted through an EDAX Pegasus Analysis system to determine the chemical composition of the samples. The EDAX system is mounted on the SEM described in the previous paragraph. EDS spectra and element mapping of samples were conducted under 20 KV with a 1.33×10^{-6} mA beam current. The elements present in the samples were quantified as oxides using the ZAF correction method available the Genesis Spectrum software.

5. Transmission Electron Microscopy

An FEI Tecnai Osiris TEM (Figure 15) was used to determine the morphology and chemical composition of obsidian and tektite crushed and LDHP samples. Crushed

(bulk) obsidian and tektite samples were dispersed in ethanol and 2–3 drops of each sample was placed on a lacey carbon-coated 400-mesh Cu TEM grid for analysis. 2–3 drops of deionized water from LDHP treatment on bulk obsidian and tektite samples were placed on a lacey carbon-coated 400-mesh Cu TEM grid, dried overnight, and analyzed. All samples were observed under 200 KV with a 0.4 mA beam current.

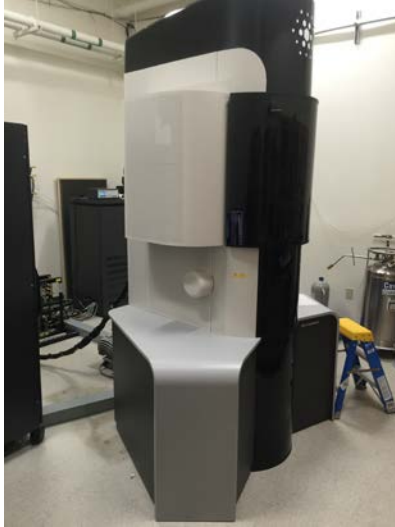


Figure 15. FEI Tecnai Osiris transmission electron microscope.

THIS PAGE INTENTIONALLY LEFT BLANK

III. RESULTS AND DISCUSSION

A. BASE MATERIAL CHARACTERIZATION

1. Obsidian

The most common color of obsidian is black, although a wide range of colors are known to exist. Its color is dependent on crystal-structured inclusions that are a part of its composition [13], [14]. Optical microscopy of the polished sections showed evidence of inclusions distributed randomly throughout the surface (Figure 16). It is possible that some large inclusions were removed from the specimen during polishing leaving the appearance of porosity; however, these may also be gas bubbles trapped during the formation of obsidian.

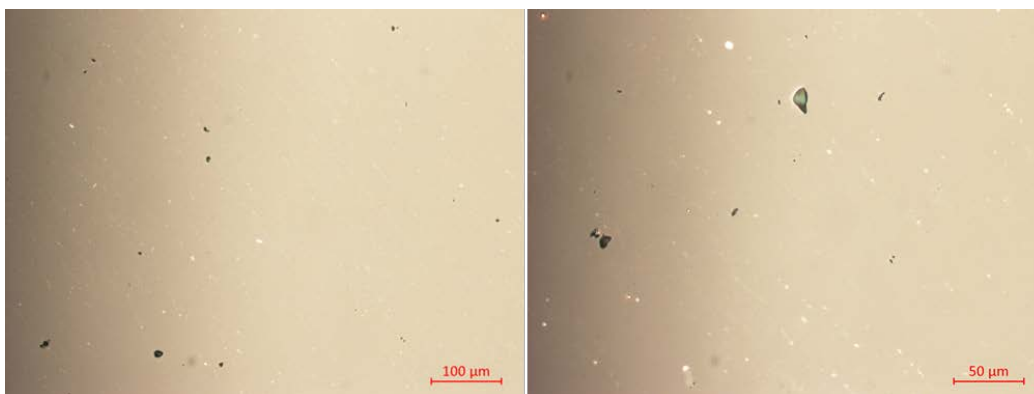


Figure 16. Optical micrographs of polished sections of bulk obsidian showing inclusions and porosity.

When a small sample of black obsidian was crushed, the resultant powder appeared light grey in color (Figure 17). This change in color may be due to larger inclusions separating from the powder during crushing. XRD analysis of the bulk and crushed obsidian samples showed an amorphous diffraction pattern with some minor peaks representing possible crystallinity (Figure 18). Quantitative XRD analyses of these patterns indicated the bulk obsidian contained 7.3% crystallinity and the crushed obsidian contained 9.5% crystallinity.

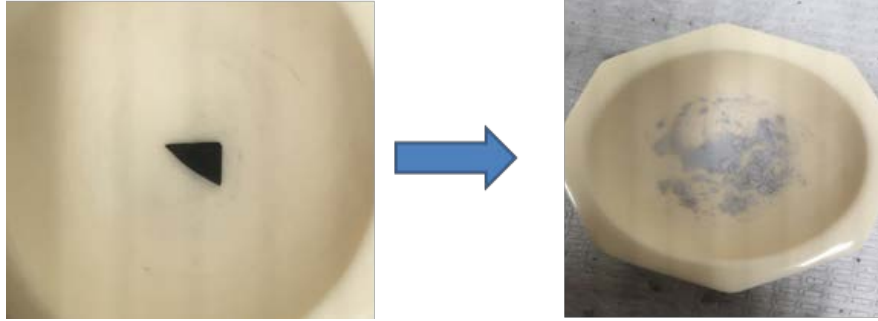


Figure 17. Images of a bulk obsidian sample before (left) and after (right) crushing with a mortar and pestle.

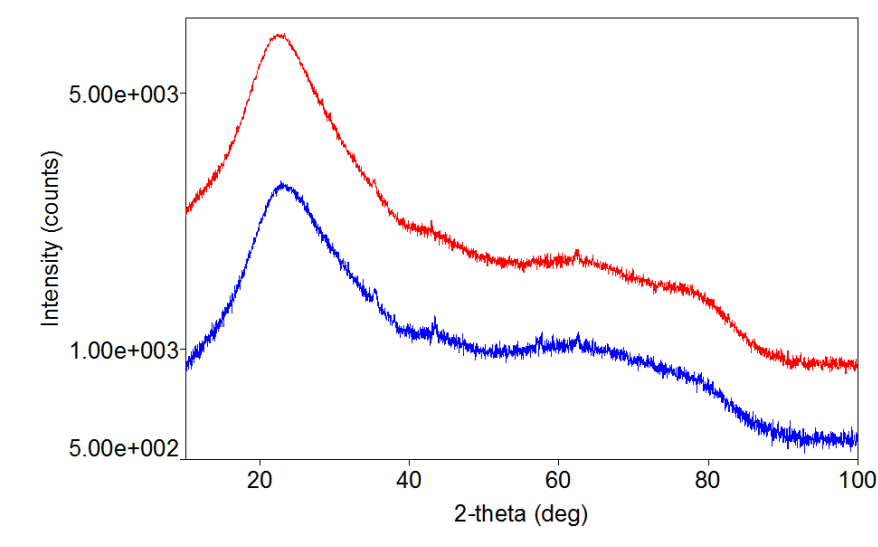


Figure 18. XRD diffraction patterns of bulk (red) and crushed (blue) obsidian samples.

EDS analysis of the bulk obsidian sample showed that this material consisted of 76.34 wt% SiO_2 with 13.21 wt% Al_2O_3 , 1.06 wt% Fe_2O_3 , and the remaining composition being made up of various oxides of Na, Mg, K, Ca, and Ti. Naturally occurring obsidian sourced from the northwestern United States contain a generally consistent chemical composition with some minor variation in its major oxides. According to Ericson et al. [10], these samples are rhyolitic obsidian having SiO_2 greater than 66 wt%. Table 2 shows the average EDS chemical composition (calculated from spectra from three different locations) of the sample bulk obsidian and is compared with the reported [10] composition of a sample of rhyolitic obsidian sourced from Mt. St.

Helena in Calistoga, CA. Figure 19 shows the EDS spectrum (20KV, 200 sec acquisition time) of the bulk obsidian sample. EDS measurement contains approximately ± 0.1 wt% error for major elements while the data in [10] is based on X-ray fluorescence spectrometry, which typically contains a ± 0.05 wt% error [15].

Table 2. Chemical composition of bulk obsidian sample and rhyolitic obsidian [7].

<i>Oxide</i>	<i>Sample Avg Composition Wt%</i>	<i>Reference Composition Wt%</i>
<i>SiO₂</i>	76.34	79.26
<i>Al₂O₃</i>	13.21	12.41
<i>K₂O</i>	5.35	3.98
<i>Na₂O</i>	2.61	4.14
<i>Fe₂O₃</i>	1.06	1.47
<i>CaO</i>	0.91	0.35
<i>TiO₂</i>	0.19	0.11
<i>MgO</i>	0.17	0.05

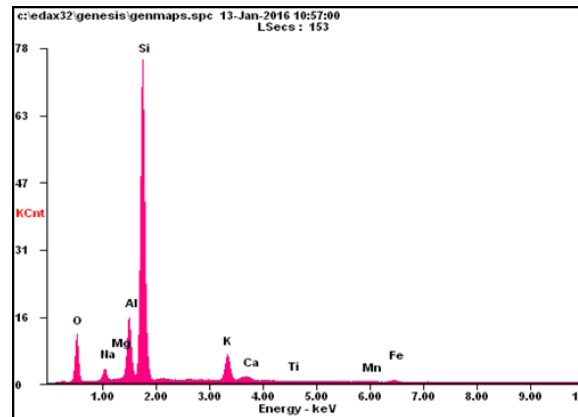


Figure 19. EDS spectrum of bulk obsidian sample.

Secondary electron images and EDS mapping of bulk and crushed obsidian samples showed micron-sized Fe-rich and Al-rich oxide particles. X-ray mapping of the bulk obsidian sample showed a 20- μ m Fe-rich oxide particle (Figure 20), while mapping of the crushed obsidian sample showed Fe-rich oxide particles in the range of 2–10 μ m

and Al-rich oxide particles ranging from 2–8 μm (Figure 21). Of note are the greater instances of large Fe-rich oxide inclusions apparent in this particular crushed sample when compared to the bulk sample.

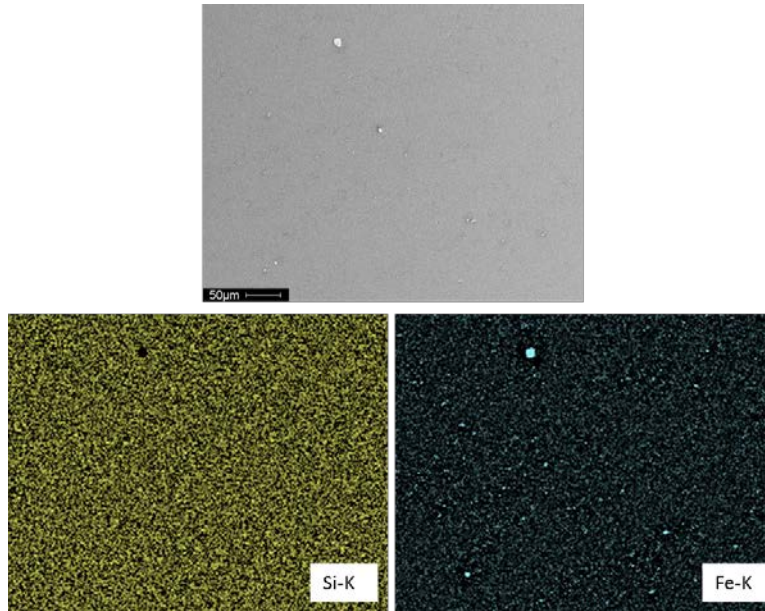


Figure 20. Secondary electron image of bulk obsidian sample (top). SEM-EDS mapping of same bulk obsidian sample showing Si distribution among the sample (bottom left) and Fe-rich oxide particles randomly distributed throughout the sample (bottom right). Note the large Fe-rich particle on the top left section of the Fe-K map.

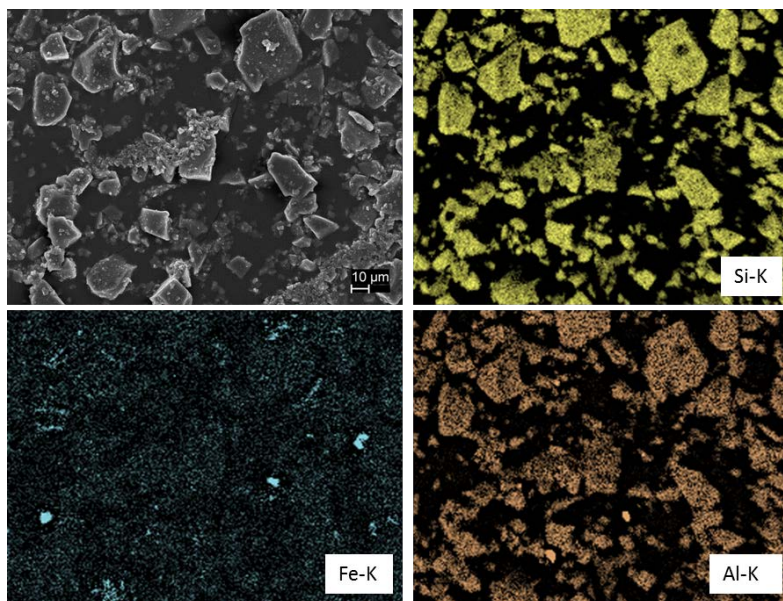


Figure 21. Secondary electron image of a crushed obsidian sample (top left). SEM-EDS mapping showing Si distribution (top right), Fe-rich oxide particles (bottom left), and Al-rich oxide particles (bottom right).

SEM-EDS analysis of the crushed obsidian samples showed a variation in its chemical composition from the bulk sample depending on the particle selected. For example, in the same secondary electron image as in Figure 21, Figure 22 shows one particle containing 73.49 wt% of Fe_2O_3 , while another particle contains 97.11 wt% (Table 3 and Figure 23 provide chemical composition and EDS spectra, respectively). This is not unexpected as the electron-sample interaction volume when using EDS makes the analysis of small particles highly influenced by the matrix elements. Thus, the EDS spectra from inclusion detached from the bulk obsidian will show the presence of Si and other elements. SEM-EDS mapping provides good qualitative results of the elemental distribution in these samples. Hence, these results support the notion of transition element-rich inclusions being separated from the bulk during crushing.

In the polished samples, the inclusions appeared as different colored particles under the optical microscope due to the absorption contrast. Upon crushing, many of these inclusions, especially the larger ones, detach from the mostly SiO_2 glassy matrix of obsidian leaving the majority of the obsidian powder to reflect most of the visible light

incident on it. Thus, the crushed powder appeared gray rather than black like the bulk sample where a large percentage of light reflected from the SiO_2 matrix is presumably absorbed by the inclusions contained within.

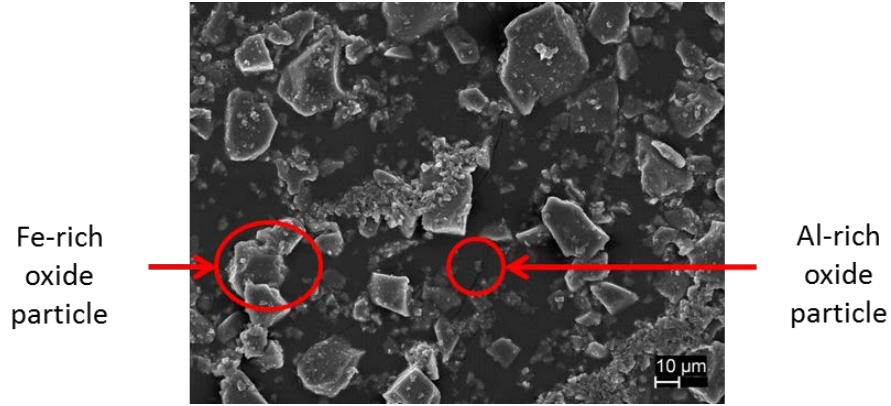


Figure 22. Secondary electron image of a crushed obsidian sample showing Fe-rich and Al-rich oxide particles circled in red.

Table 3. Chemical composition of Fe-rich and Al-rich oxide particles from Figure 22.

<i>Oxide</i>	<i>Fe-rich particle Wt%</i>	<i>Al-rich particle Wt%</i>
<i>SiO₂</i>	19.31	1.66
<i>Al₂O₃</i>	3.74	97.11
<i>K₂O</i>	1.52	0.07
<i>Na₂O</i>	0.53	0.40
<i>Fe₂O₃</i>	73.49	0.04
<i>CaO</i>	0.83	0.03
<i>TiO₂</i>	0.54	0
<i>MgO</i>	0.05	0.69

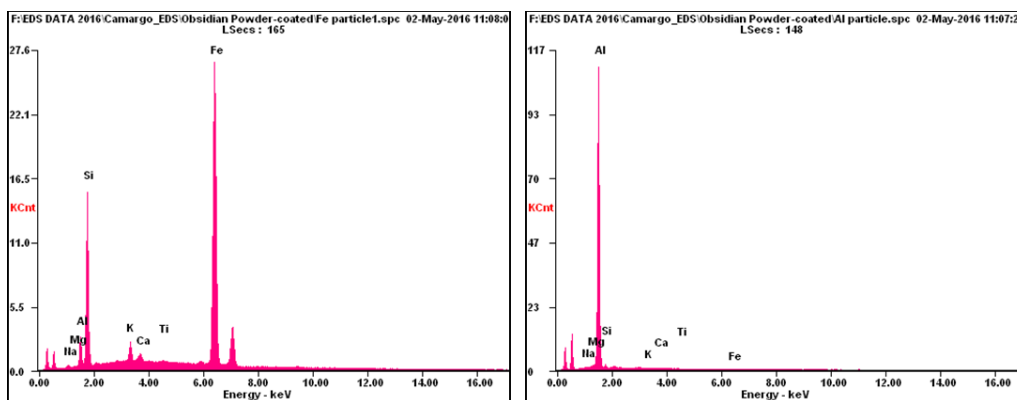


Figure 23. SEM-EDS spectra of a Fe-rich oxide particle (left) and Al-rich oxide particle (right).

TEM analysis of the crushed obsidian sample provided bright field scanning transmission microscopy (BF-STEM) and high-angle annular dark field scanning transmission electron microscopy (HAADF-STEM) images (Figure 24). In Figure 24, BF-STEM images show heavy elements in dark contrast while HAADF-STEM images provide bright contrast to elements with high atomic number. In these images, the obsidian particles appear as mostly large and thin fragments with sharp edges due to the glassy nature. The dark contrast in the BF-STEM images and the corresponding bright contrast in the HAADF-STEM images arise from the mass thickness as well as atomic number contrast (Z-contrast). From these images alone, it is difficult to conclude the nature of these fine particles. As an example, three particles marked with arrows 1, 2, and 3 are discussed. Scanning transmission electron microscopy energy dispersive X-ray spectroscopy (STEM-EDS) mapping of this area is therefore very useful in providing additional information towards understanding the nature of these regions. STEM-EDS mapping showed nm-sized oxide particles rich in Ti, Fe, and Al within larger SiO_2 particles. In Figure 25, STEM-EDS mapping shows Ti-rich oxide particles in the range of 40–80 nm and 700-nm Al-rich oxide particle. This evidence suggested that bulk obsidian contains various oxides embedded within its amorphous SiO_2 matrix. Clearly, particle 1 is a fine nm-sized piece of SiO_2 , particle 2 in an Al-rich particle presumed to be Al_2O_3 , and particle 3 is a Ti-rich particle presumed to be TiO_2 . Many such areas were examined by STEM-EDS and nm-sized oxide inclusions enriched in Na, Al, Ti, or Fe were evident.

Figure 26 provides STEM-EDS mapping of another area showing particles rich in Si (400 nm in size) and Fe (80 nm in size).

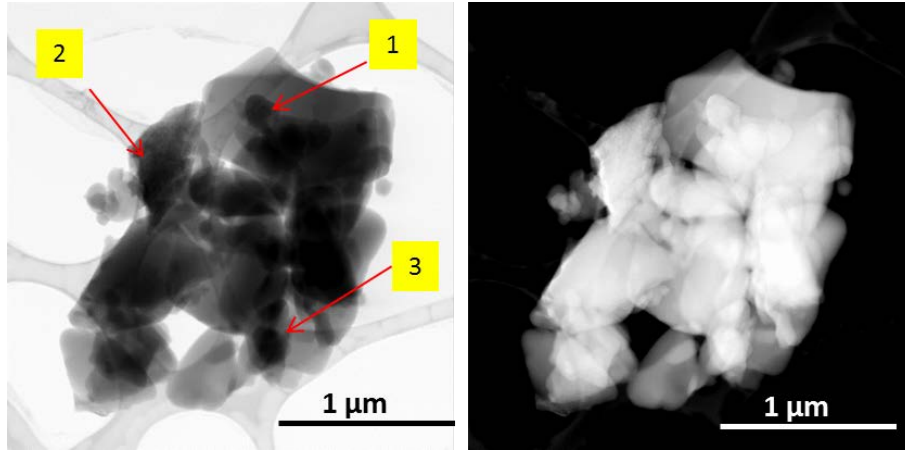


Figure 24. BF-STEM (left) and HAADF-STEM (right) images of crushed obsidian sample particles.

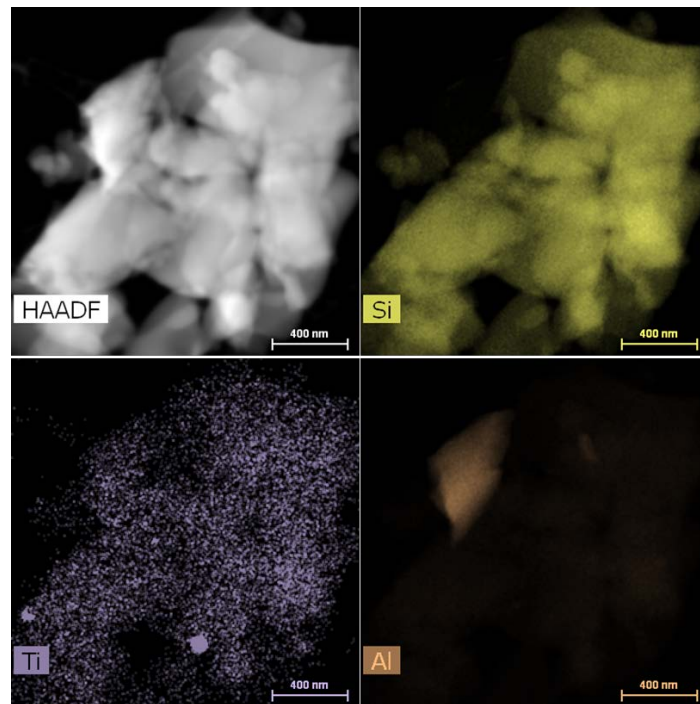


Figure 25. STEM-EDS mapping showing oxide particles rich in Si (top right), Ti (bottom left), and Al (bottom right).

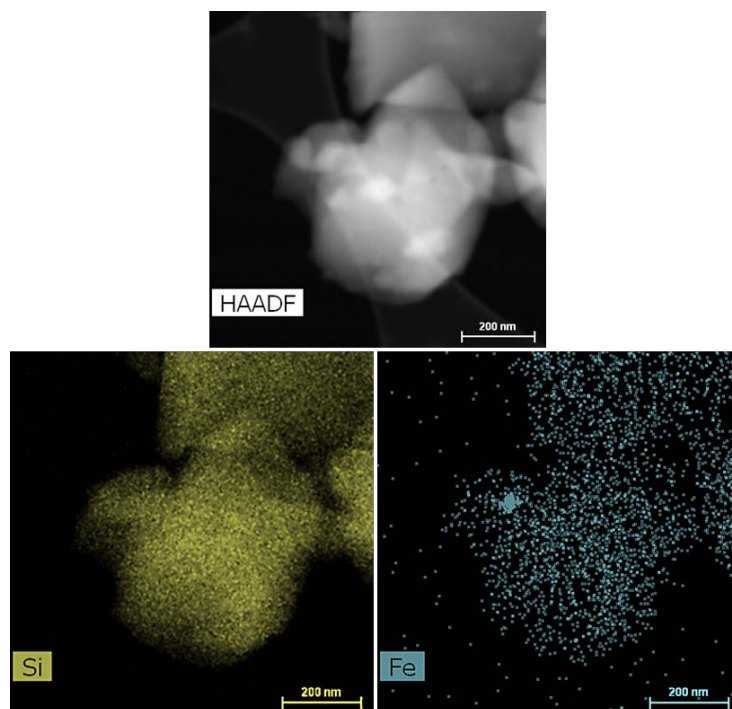


Figure 26. STEM-EDS mapping showing oxide particles rich in Si (bottom left) and Fe (bottom right).

2. Tektite

Like obsidian, the color of tektite also depends on the crystal-structured inclusions embedded in its composition with the basic color being green or greenish-blue and some in black or brown [16]. Optical microscopy showed the absence of inclusions, however porosity was clearly evident throughout the samples (Figure 27).

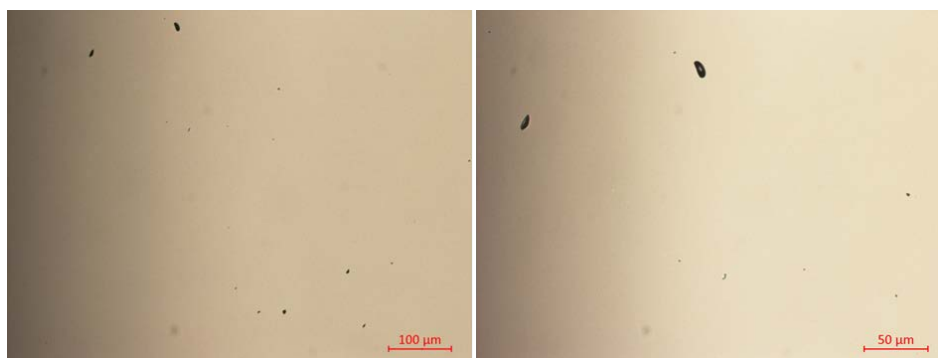


Figure 27. Optical Micrographs of Polished Sections of Bulk Tektite Samples showing Porosity.

When the black tektite sample was crushed with a mortar and pestle, the resultant powder also appeared grey in color, but with a hint of yellow (Figure 28). XRD analysis of a bulk and crushed tektite sample also showed an amorphous diffraction pattern with few minor peaks (Figure 29). In this case, Figure 29 shows that these samples appeared to be fully amorphous and is likely that the small volume fraction in these samples were too small to be detected by XRD. Further quantitative XRD analyses of these patterns indicated the bulk tektite contained 1.3% crystallinity and the crushed tektite contained 7.4% crystallinity. However, a separate bulk tektite sample showed the majority being crystalline in structure with calcite (CaCO_3), aluminum silicate ($\text{Al}_2\text{O}_3\text{-SiO}_2$), and sodium aluminum silicate ($\text{Na}_{1.15}\text{Al}_{1.15}\text{Si}_{0.85}\text{O}_4$) as the identified peaks (Figure 30). In this particular sample, the crystallinity was determined to be 70%. This observation suggests this sample's inhomogeneity is a result of how these materials are formed [17]. Thus, some areas contained high amounts of minerals (crystalline) while other areas are almost purely glassy in nature.

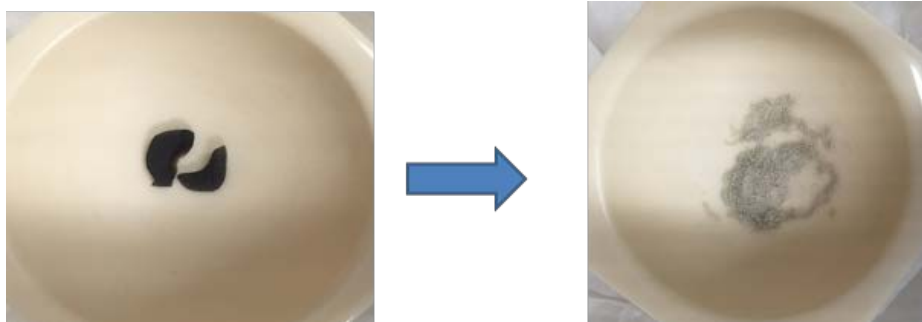


Figure 28. Images of a bulk tektite sample before (left) and after (right) crushing with a mortar and pestle.

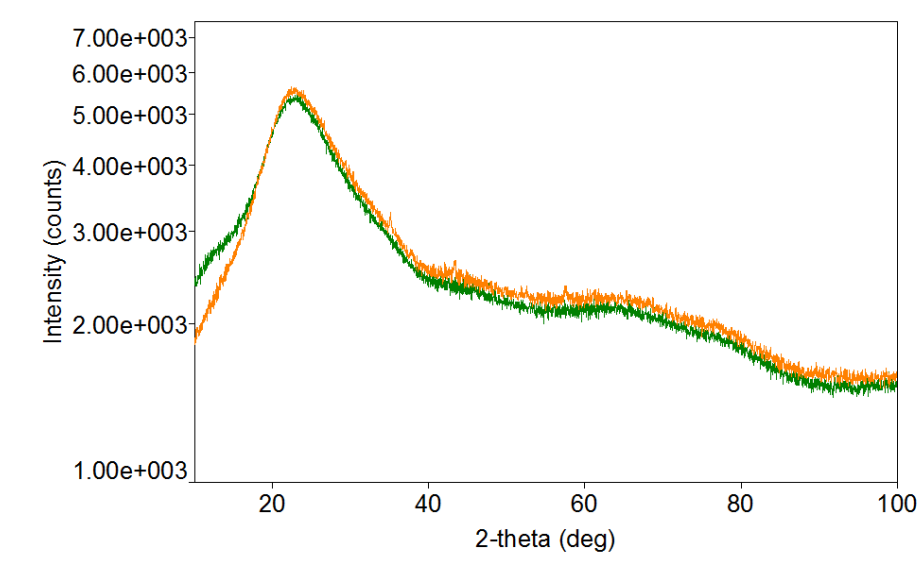


Figure 29. XRD diffraction patterns of bulk (green) and crushed (orange) tektite samples.

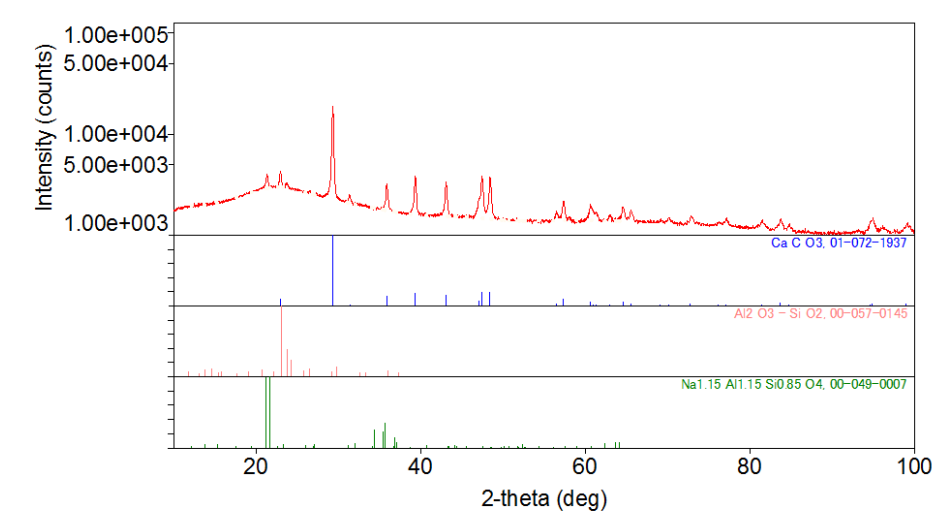


Figure 30. XRD diffraction pattern of bulk tektite sample with 70% crystallinity.

SEM-EDS analysis of the bulk tektite sample in this study showed this material consists of 73.04 wt% SiO_2 with 12.34 wt% Al_2O_3 , 5.98 wt% FeO , and the remaining composition being made up of various oxides. Tektites from Indonesia come from the Australasian strewn field, which is comprised of Australia, Thailand, Laos, Cambodia, Vietnam, Indonesia, and Philippines [18]. According to Chapman [19], tektites from the

Australasian strewn field showed minor variations in their major oxide composition depending on the locality the sample originated from. Table 4 shows the average EDS chemical composition (calculated from spectra from three different locations) of the bulk tektite sample and a sample of Australasian tektite from Java (Note: FeO was used in this table to compare the sample with the reference, future chemical compositions will use Fe₂O₃). Figure 31 shows the EDS spectrum (20KV, 200 sec acquisition time) of the bulk tektite sample. In this study, compared to obsidian, tektite appeared richer in Fe, Ti, Ca, and Mg, but poorer in Na and K. These differences in compositions may be related to volcanic origin of obsidian and the formation of tektite from meteoritic impact on the surface of the earth, to include the geographic areas where these events occur.

Table 4. Chemical composition of bulk tektite sample and tektite sample J71 Sangiran Java [19].

<i>Oxide</i>	<i>Sample Avg Composition Wt%</i>	<i>Reference Composition Wt%</i>
<i>SiO₂</i>	73.04	72.00
<i>Al₂O₃</i>	12.34	12.00
<i>FeO</i>	5.98	5.32
<i>K₂O</i>	2.54	2.26
<i>CaO</i>	2.05	2.85
<i>MgO</i>	2.34	3.19
<i>TiO₂</i>	0.90	0.68
<i>Na₂O</i>	0.76	1.31

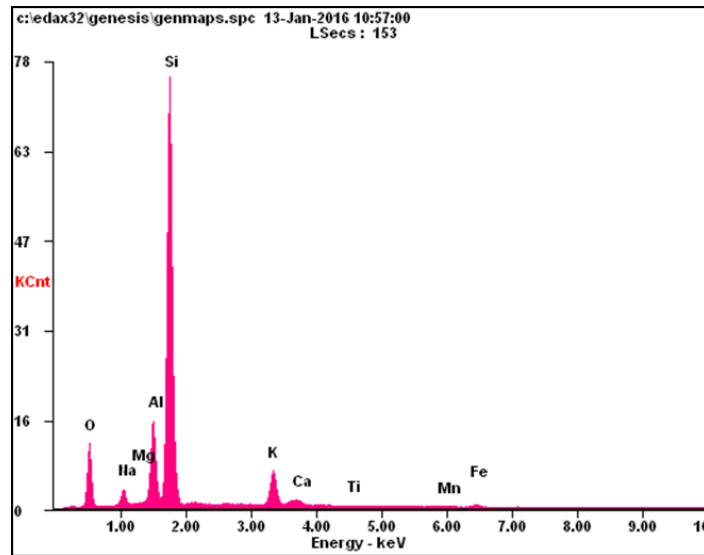


Figure 31. EDS Spectrum of Bulk Tektite Sample.

Secondary electron images and EDS mapping of the crushed tektite sample showed micron-sized Fe-rich and Al-rich oxide particles. Mapping of the bulk tektite sample in the SEM did not show any oxide particles rich in transition elements in the areas analyzed. It was presumed due to the sparse nature of large inclusions in tektite, it was difficult to locate inclusions on the sample surface. Figure 32 shows secondary electron images of the surface of a bulk tektite sample with evidence of porosity (as indicated by red arrows). Similar to the bulk obsidian sample, some of these pores may have contained inclusions that possibly fell out during sample preparation. Figure 33 shows SEM-EDS maps of the crushed tektite sample with a 4- μm Fe-rich oxide particle and two Al-rich oxide particles approximately 3–4 μm in size. As in the case of obsidian, this observation also suggests the separation of heavy element-rich inclusions being separated from the bulk during crushing of tektite.

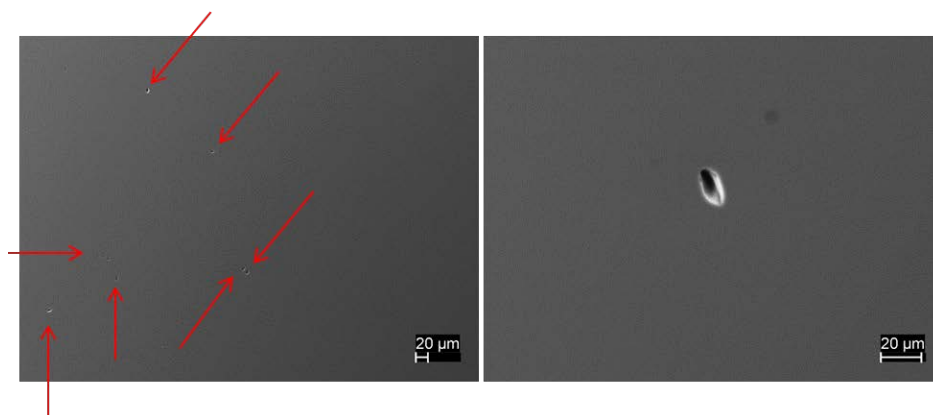


Figure 32. Secondary electron images showing porosity in the surface of a polished bulk tektite sample.

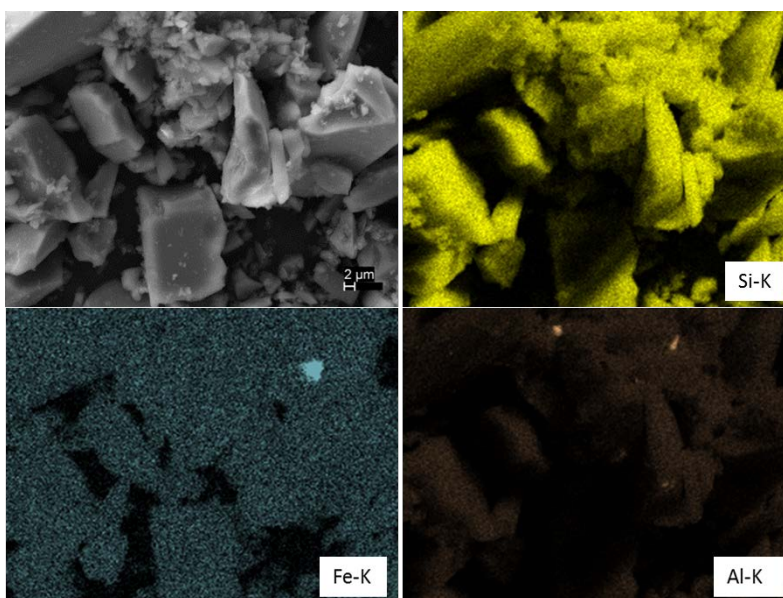


Figure 33. Secondary Electron image of a crushed tektite sample (top left). SEM-EDS mapping showing Si distribution (top right), Fe-rich oxide particle (bottom left), and Al-rich oxide particles (bottom right).

Figure 32 provides two secondary electron images of two distinct areas of the crushed sample. EDS analysis was performed on the entire area of Figure 34(a) and on a section of a crushed tektite particle (red box in Figure 34(b)). Quantitative EDS analysis of the bulk tektite sample and the two areas in Figure 32 showed a slight variation of all the oxides listed in its chemical composition compared to the bulk tektite sample (Table

5). Figure 35 shows the EDS spectra of the crushed tektite sample and crushed tektite particle, which appear nearly identical. These observations indicate that the act of crushing mostly turns the bulk tektite into smaller particles of similar chemical composition. Additionally, the separation of transition element-rich inclusions during crushing may explain the variation of the chemical composition observed in these samples.

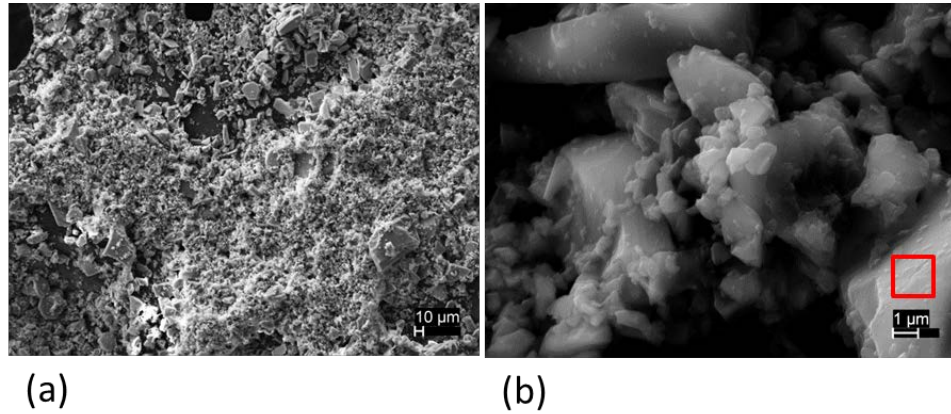


Figure 34. Secondary electron images showing (a) area of crushed tektite and (b) crushed tektite particle analyzed. Red box indicates particle analyzed for Table 4 and Figure 35.

Table 5. Chemical Composition Comparison between Bulk Tektite, Crushed Tektite Area, and Crushed Tektite Particle.

<i>Oxide</i>	<i>Bulk Tektite Wt%</i>	<i>Crushed Tektite Area Wt%</i>	<i>Crushed Tektite Particle Wt%</i>
<i>SiO₂</i>	72.54	69.90	70.89
<i>Al₂O₃</i>	12.31	12.59	12.38
<i>Fe₂O₃</i>	6.60	8.19	6.82
<i>K₂O</i>	2.52	2.62	2.52
<i>CaO</i>	2.03	2.38	3.77
<i>MgO</i>	2.36	2.37	2.28
<i>TiO₂</i>	0.89	1.06	0.85
<i>Na₂O</i>	0.75	0.89	0.48

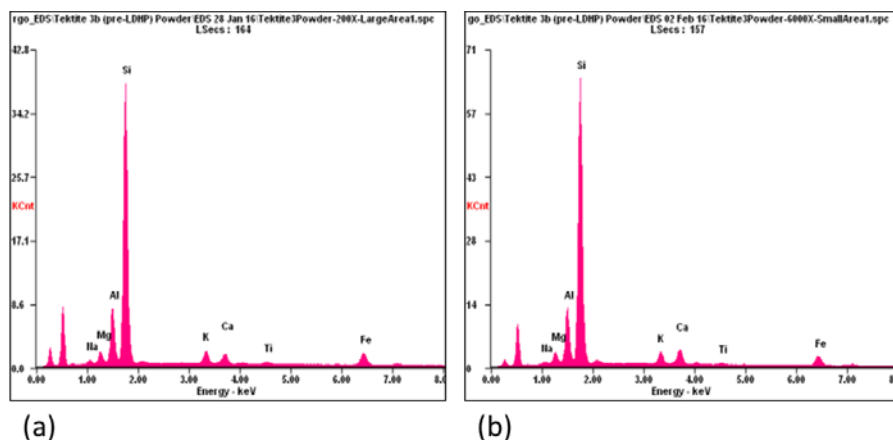


Figure 35. SEM-EDS spectra of (a) crushed tektite area and (b) crushed tektite particle corresponding to Figure 32.

TEM analysis of the crushed tektite sample BF-STEM and HAADF-STEM images (Figure 36) with particles that appeared to contain transition elements as a result of the contrast among the particles. As shown in Figure 36, particle 1 is a nm-sized piece of SiO_2 , particle 2 is Ti-rich particle presumed to be TiO_2 , and particle 3 is a an Al-rich particle presumed to be Al_2O_3 . Figure 37 shows the corresponding STEM-EDS maps to Figure 36 with several larger particles rich in Si ranging from 250–600 nm, multiple Ti-rich oxide particles in the range of 80–100 nm and two Al-rich oxide particles in 100–400 nm range. STEM-EDS maps did not show any Fe-rich particles in the various areas analyzed, but similar to the crushed obsidian sample, did show nm-sized oxide inclusions enriched in Na, Al, or Ti. This observation also suggested that bulk tektite contains various oxides embedded within the amorphous SiO_2 matrix.

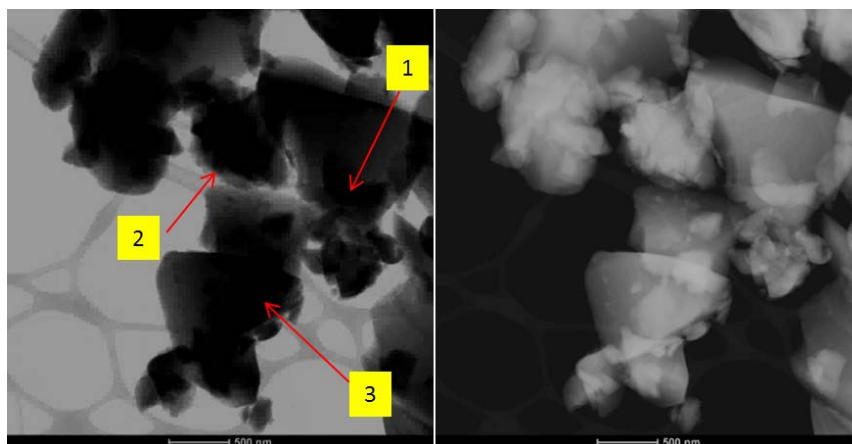


Figure 36. BF-STEM (left) and HAADF-STEM (right) images of crushed tektite particles. Scale bar 500 nm.

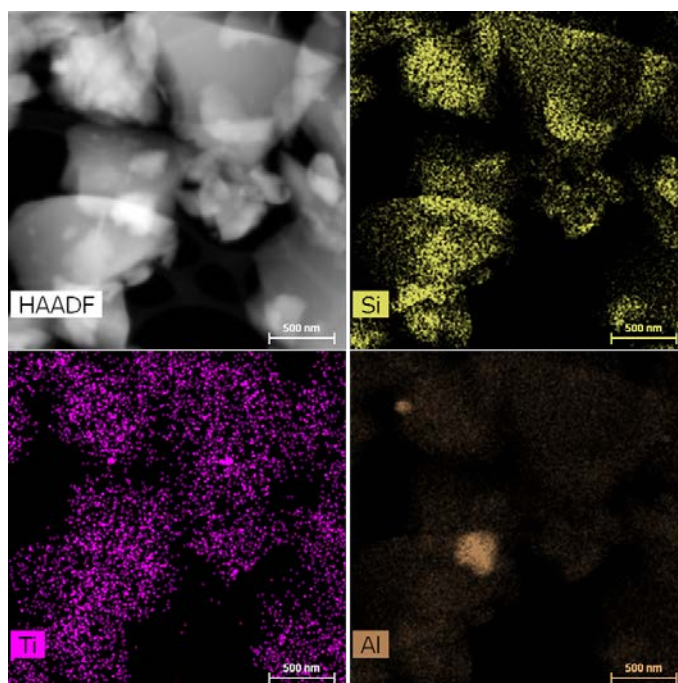


Figure 37. STEM-EDS mapping showing oxide particles rich in Si (top right), Ti (bottom left), and Al (bottom right).

B. POST-LDHP MATERIAL CHARACTERIZATION

1. Obsidian

a. *Studies on Sample Surface after LDHP*

Figure 38 shows the effects of LDHP treatment on obsidian (sample ID B7). Each treated area (six in total) in this sample was exposed to 5,000 pulses from an excimer laser using the following parameters: 248-nm laser, varying fluence, 0.6 J/pulse, and 25-ns pulse duration (shooting sequence with area 1 using the least fluence and area 6 using greatest fluence) [20]. Laser energy was maintained at approximately 0.6 J, but spot area was adjusted so that the fluence ranged from approximately 2 - 10 J/cm². At none of these fluences were the 248-nm laser pulses efficient in removing material. As can be seen from the photograph in Figure 38, LDHP produces craters on the sample surface with a few small areas left optically white/translucent. SEM analysis of the treated areas clearly show the removal of material from the sample surface (Figure 39). At lower magnification, each crater showed similar characteristics of what appears to be a spallation effect evidenced by pits and cleavage-like marks where the laser pulses presumably struck the surface (Figure 39(a)) removing material. It is assumed that the appearance of deeper/larger pits is a result of multiple laser pulses striking the same area. At higher magnification, relatively long (> 50 µm) and thin (< 1 µm) cuts were visible within the treated areas (Figure 39(c)) along with the appearance of material solidification after melting (Figure 39(d)). At these particular laser parameters, it appeared laser pulses may have raised the temperature enough to melt the material and penetrate the bulk. Given the number of laser pulses striking the surface, the surface of the material may have increased in temperature over the course of laser processing. This may have enabled laser pulses towards the end of processing to create these cuts.

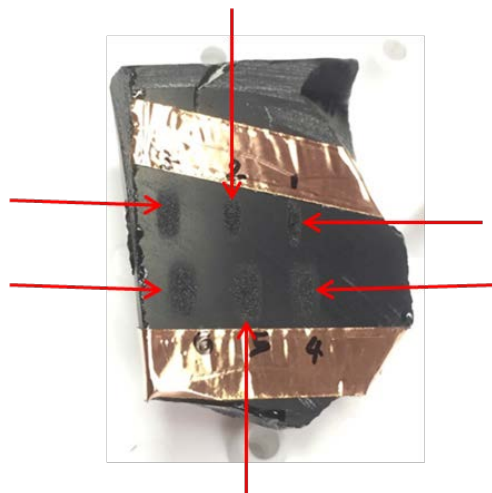


Figure 38. Post-LDHP obsidian (sample ID B7) showing six areas (red arrows) exposed to 5000, 248-nm laser pulses per crater.

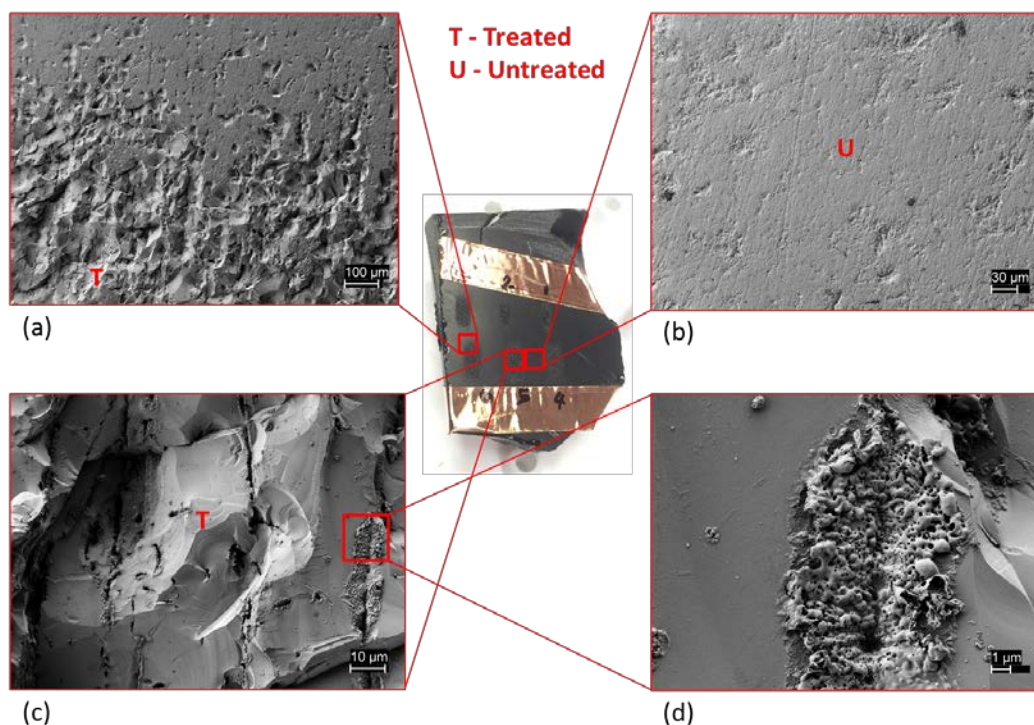


Figure 39. Secondary electron images showing effects of LDHP treatment on the surface of obsidian (sample ID B7). (a) Border of treated area 6. (b) Untreated surface between treated areas 4 and 5. (c) Increased magnification in the center of treated area 5 showing cuts presumably made by laser pulses. (d) Increased magnification of section in (c) showing the appearance of material solidification after melting.

Figure 40 shows the effects of LDHP on obsidian (sample ID B9) using a different set of laser parameters. This area was exposed to 300 pulses from a frequency-tripled neodymium-doped yttrium lithium fluoride and aluminum-phosphate glass-1 (Nd:YLF&APG1) laser using the following parameters: 351-nm laser, 3.5 J/cm^2 fluence, and 15-ns pulse duration [20]. LDHP parameters used on this sample left the entire treated area optically white/translucent with what appeared to be small, colorless crystals. EDS analysis performed on the untreated and treated areas showed a slight change among the major oxides (Table 6 and Figure 41). This change may be attributed to the typical minor variation seen in the chemical composition throughout obsidian.

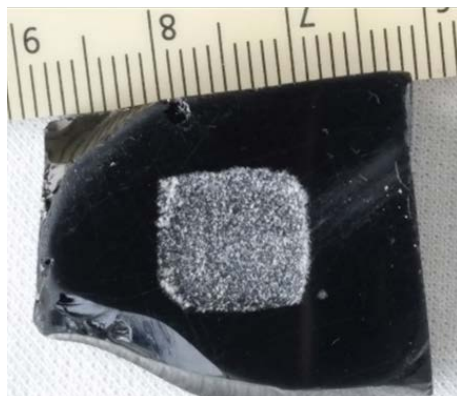


Figure 40. Image of LDHP treatment on surface of obsidian (sample ID B9). Treated area optically white/translucent in color from exposure to 300, 351-nm pulses.

Table 6. Comparison of chemical composition between untreated and LDHP treated areas of obsidian sample B9.

<i>Oxide, Wt%</i>	<i>Untreated</i>	<i>Treated</i>
<i>SiO₂</i>	77.94	77.3
<i>Al₂O₃</i>	11.77	11.7
<i>K₂O</i>	5.86	6.02
<i>Na₂O</i>	2.25	2.55
<i>Fe₂O₃</i>	1.31	1.36
<i>CaO</i>	0.85	0.88
<i>TiO₂</i>	0.09	0.12
<i>MgO</i>	0.01	0

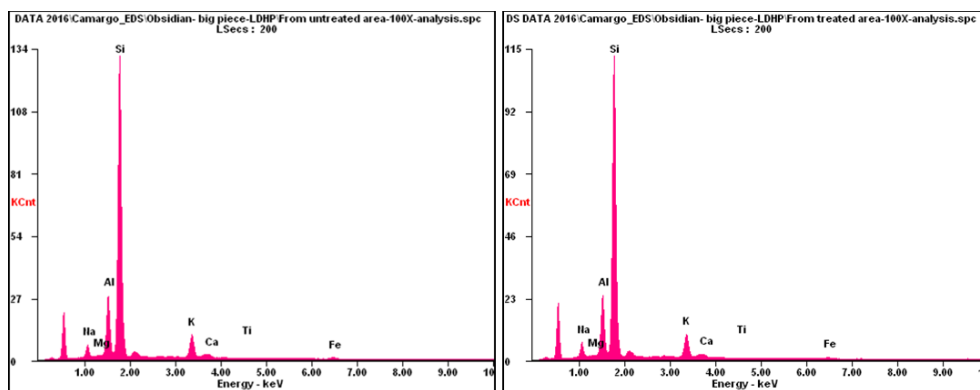


Figure 41. EDS spectra of obsidian sample B9 showing untreated area (left) and LDHP treated area (right).

b. Studies on Particles in Deionized Water after LDHP

In a separate LDHP experiment, an obsidian sample (sample ID BC14) submerged in deionized water was targeted with 200 laser pulses using an Nd:YLF&APG1 glass laser with the following laser parameters: 1053-nm laser, 5 J/cm² fluence, and 17-ns pulse duration [20]. After completion of this experiment, heavier particles that accumulated on the bottom of the LDHP apparatus was collected and left to air dry on a paper sheet overnight for analysis. As an example, Figure 42 shows an image of particles from an LDHP experiment on a separate obsidian sample not analyzed in this study. As seen in the image, these particles appeared optically white/translucent.

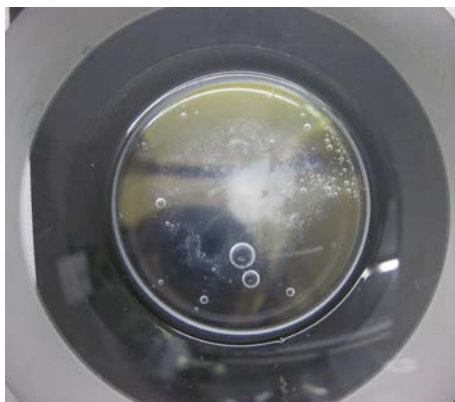


Figure 42. Image of particles collected from post-LDHP treatment on obsidian sample. Note the optically white/translucent appearance of the particles. Source: [21].

The particles generated from the obsidian sample (sample ID BC14) used in this study also appeared optically white/translucent. Secondary electron images and EDS analysis showed Si-rich oxide particles ranging from 1–25 μm and Fe-rich oxide particles ranging from 1–5 μm in size (Figure 43). Figure 44 shows two particles (as indicated by the red box), each from two different areas in the same sample, analyzed for chemical composition. Table 7 and Figure 45 provide the results of the EDS analysis and show a similar chemical composition with some variation in oxides. When compared to the bulk obsidian sample studied earlier, this suggests LDHP, like crushing, turns the bulk material into smaller particles of similar chemical composition.

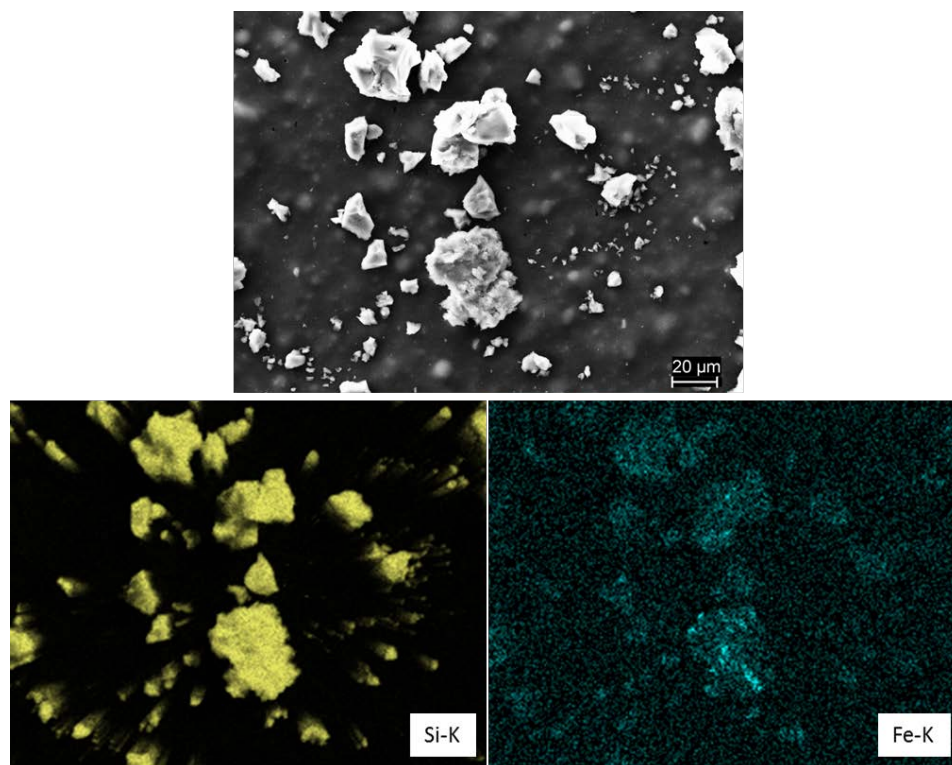


Figure 43. Secondary electron image of post-LDHP obsidian particles collected from sample BC14 (top). SEM-EDS mapping showing Si distribution (bottom left) and Fe-rich oxide particles (bottom right).

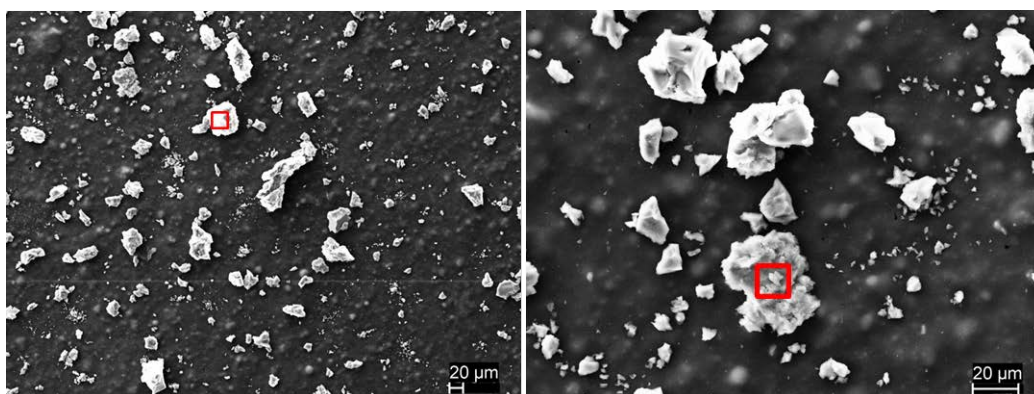


Figure 44. Secondary electron images showing two different post-LDHP obsidian particle areas from sample BC14 at x150 magnification (left) and x500 magnification (right). Red boxes indicate particle 1 (left) and particle 2 (right) analyzed for Table 6.

Table 7. Comparison of chemical composition between bulk obsidian sample, post-LDHP particle 1, and post-LDHP particle 2.

<i>Oxide</i>	<i>Bulk Obsidian Wt%</i>	<i>Post-LDHP Obsidian Particle 1 Wt%</i>	<i>Post-LDHP Obsidian Particle 2 Wt%</i>
<i>SiO₂</i>	76.34	74.77	77.12
<i>Al₂O₃</i>	13.21	12.24	13.74
<i>K₂O</i>	5.35	7.92	2.29
<i>Na₂O</i>	2.61	1.82	4.3
<i>Fe₂O₃</i>	1.06	1.11	1.2
<i>CaO</i>	0.91	1.46	1.05
<i>TiO₂</i>	0.19	0.49	0.09
<i>MgO</i>	0.17	0.2	0.22

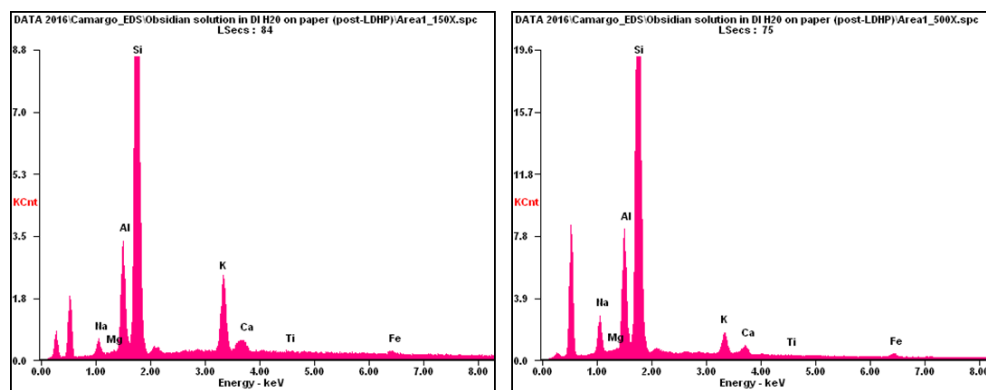


Figure 45. EDS spectra of particle 1 (left) and particle 2 (right) from post-LDHP obsidian particle sample BC14.

TEM analysis was conducted on the suspended particles in deionized water (sample ID BC14SN) collected after the same LDHP experiment described earlier on obsidian sample BC14. BF-STEM and HAADF-STEM images (Figure 46) on this sample showed that many fine particles are present in the deionized water after LDHP. In general, there were many particles that appeared to contain heavy elements. STEM-EDS maps (Figure 47) showed these particles rich in Si and Al 400 nm in size, multiple Ti-rich oxide particles in the range of 50–200 nm, and multiple Fe-rich oxide particles ranging in 100–300 nm. From Figure 46, particle 1 is presumed to contain SiO₂ and Al₂O₃, particles

labeled 2 are presumed to be TiO_2 and the three particles labeled 3 are presumed to be Fe_2O_3 . Generally, particles rich in Si were observed to have a polyhedral/angular morphology and were observed mostly as particles closer to 1 μm in size. Ti-rich particles were observed in spheroidal shapes usually in the 150–500 nm range and often in small clusters. Fe-rich particles were observed in a large size range, 50 nm – 1 μm , typically in a spheroidal shape, and also observed in small clusters. Finally, particles rich in Al were observed in the 25–500 nm size range, in polyhedral/angular shapes, and often in the upper end of the size range in small clusters. The general observation was that there were a greater number of transition element-rich oxide particles in this sample compared to the number of Si-rich oxide particles.

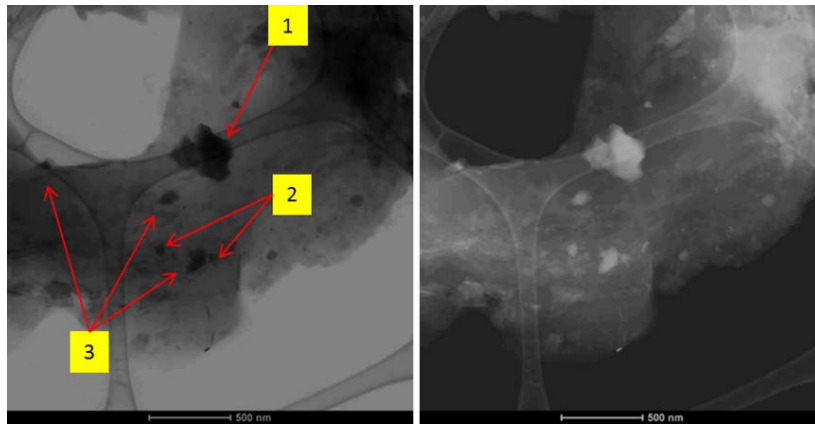


Figure 46. BF-STEM (left) and HAADF-STEM (right) images of post-LDHP obsidian particles in sample BC14SN. Scale bar 500 nm.

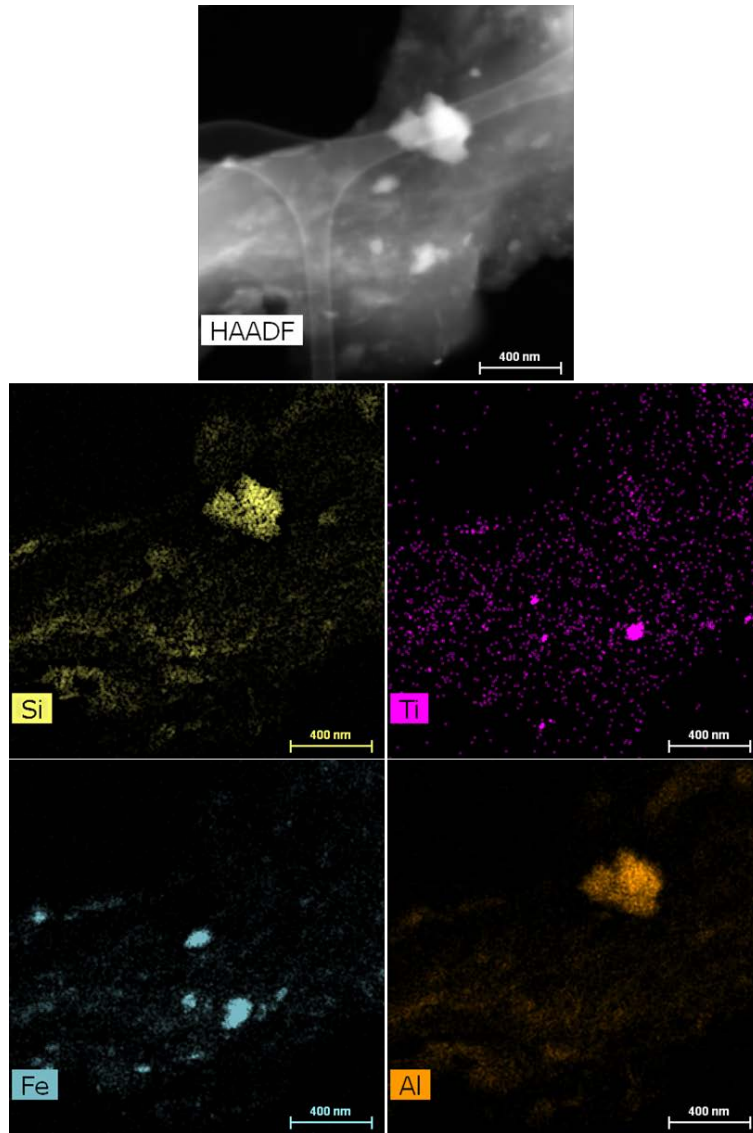


Figure 47. STEM-EDS mapping of post-LDHP obsidian particles in sample BC14SN showing oxide particles rich in Si (middle left), Ti (middle right), Fe (bottom left) and Al (bottom right).

High-resolution transmission electron microscopy (HRTEM) images of the same sample clearly showed particles with crystallinity. An example of an 80-nm inclusion contained in a relatively large obsidian particle is shown in Figure 48(a). Figure 48(b) shows the inclusion at an increased magnification with an 18-nm particle clearly defined at its outer edge. Figure 48(c) shows the outer edge of the 18-nm particle at increased magnification displaying lattice fringes and embedded in an amorphous matrix. Figure 49

shows the analysis of a different particle in the same sample. Using Digimicrograph software, the lattice plane spacing was measured and the average value of these lattice planes was determined to be 0.254 nm. Further investigation reveals that this plane spacing indicates a type of iron oxide. Diffraction data software provided potential candidates to identify the specific type of iron oxide, however it is inconclusive to pinpoint the oxide since the particles were exposed to water for an extended period of time and the oxidation state might have changed:

1. FeO in $\langle 111 \rangle$ direction (0.2533 nm d-spacing)
 2. Fe₂O₃ in $\langle 110 \rangle$ direction (0.2519 nm d-spacing)
 3. Fe₃O₄ in $\langle 311 \rangle$ direction (0.2498 nm d-spacing)
- *Fe in $\langle 111 \rangle$ direction (0.2125 nm d-spacing)

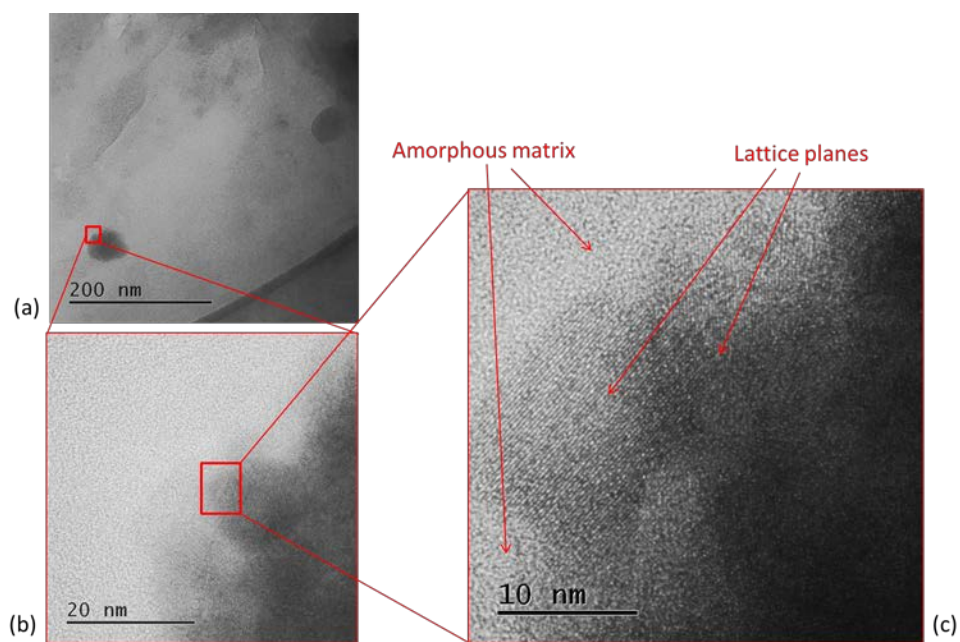


Figure 48. HRTEM images showing crystallinity in a particle among an amorphous matrix from post-LDHP obsidian particles in sample BC14SN. (a) 80-nm inclusion within post-LDHP obsidian particle. (b) Increased magnification of outer edge of inclusion in (a) showing 18-nm particle. (c) Increased magnification of outer edge of particle in (b) showing lattice planes with average plane spacing determined to be 0.254 nm.

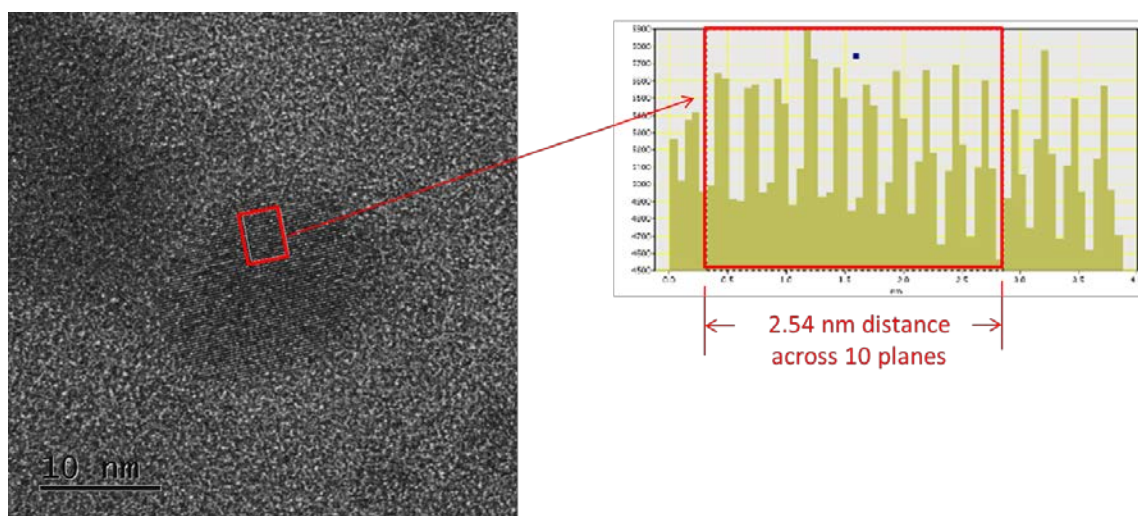


Figure 49. HRTEM image of particle with crystallinity from post-LDHP obsidian in sample BC14SN. Red box indicates area measured to determine chemical compound based on plane spacing.

These results suggest that the fine inclusions in these samples are crystalline and that the Fe-rich inclusions are one of the iron oxide.

In summary, the bulk obsidian is mostly of the amorphous silica with smaller quantities of crystalline oxides in some variation. A color change was observed from black in its bulk form to light grey when crushed, suggesting the separation of embedded inclusions. SEM-EDS mapping of bulk and crushed forms showed micron-sized oxide particles rich in Fe and Al as small as 2 μm and as large as 20 μm . STEM-EDS mapping of the crushed obsidian showed nm-sized oxide particles rich in Si, Ti, Fe, and Al, between 40–800 nm, typically within larger SiO_2 particles.

Each bulk obsidian sample showed the formation of craters after LDHP treatment. SEM analysis of the craters showed cleavage-like marks suggesting spallation. Also observed was the appearance of material solidification after melting in the form of long, thin cuts within the craters on one sample. Optically white/translucent remnants with crystals on the treated surface were observed. Formation of the observed crystals suggests removed material, possibly in ionic form, precipitating and redeposited onto the surface. The larger/heavier particles collected after LDHP also appeared optically white/translucent. SEM-EDS analysis showed oxide particles rich in Si and Fe ranging from 1–25 μm , while analysis of other oxide particles showed a similar chemical composition to bulk obsidian. STEM-EDS mapping of the suspended particles showed greater quantities of what is presumed to be oxide particles rich in Si, Fe, Ti, and Al as small as 25 nm up to 1 μm . Overall, two general observations were made from these results: (i) fewer micron-sized SiO_2 particles with various oxides embedded within and (ii) greater number of nm-sized oxide particles rich in Fe, Ti, and Al. When compared to analysis performed on the crushed samples, this observation also suggests the spallation effect of LDHP and the possible formation of precipitates.

2. Tektite

a. Studies on Sample Surface after LDHP

Figure 50 demonstrates the effects of LDHP treatment on tektite (sample ID 21DEC15 Tektite). Areas 1 and 2 in this sample were exposed to 100 pulses and area 3

was exposed to 200 pulses from a neodymium-doped yttrium aluminum garnet (Nd:YAG) laser using the following parameters: 1065-nm laser, 40 J/cm² fluence, 2.6 J/pulse, and 10-μs pulse duration [20]. In comparison to LDHP treatment on obsidian with a different set of laser parameters, a noticeable difference was observed in the appearance and depth of the craters. Areas 1 and 2 were measured at a depth of 643.61 μm and 636.42 μm, respectively, and area 3 at 971.68 μm (measurements were performed with a Keyence VHX-5000 optical imaging profilometer at LLNL [22]). With relatively the same depth in craters 1 and 2, and a nearly 300 μm increase in depth in crater 3, the difference was attributed to the 100-pulse increase used in area 3. Additionally, the surface of each crater showed the appearance of colorless crystals. Figure 51 shows an image of the crystals in crater 3 as an example.

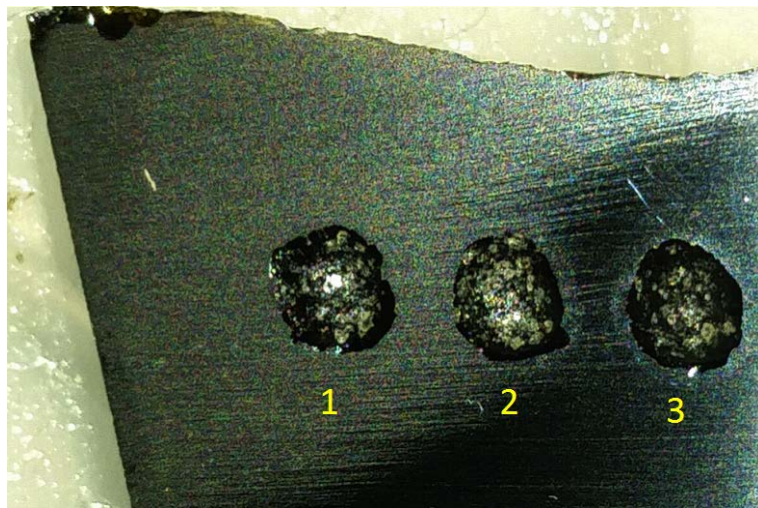


Figure 50. Post-LDHP tektite showing three areas exposed to 100 (1 and 2) and 200 (3), 1065-nm laser pulses per crater. Source: [22].

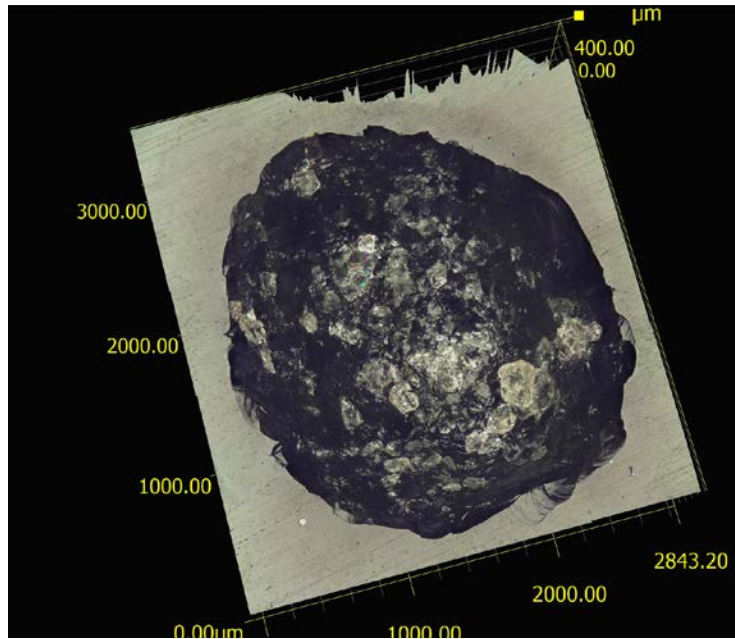


Figure 51. Image of crater 3 showing the appearance of crystals in post-LDHP tektite sample. Image captured by a Keyence VHX-5000 optical imaging profilometer at LLNL. Source: [20].

SEM analysis of the treated areas showed material removed from the sample surface (Figure 52). At lower magnification, each crater showed similar characteristics of cleavage-like marks where the laser pulses presumably struck the surface. At higher magnification, there appears to be holes approximately 3–6 μm in diameter surrounded by evidence of re-solidified material after melting (Figure 53). Similar to the post-LDHP obsidian, these laser parameters may have also raised the temperature enough to melt the material and penetrate the bulk. Although a significantly less number of laser pulses were used on this sample, the surface of the material may have increased in temperature over the course of the laser processing. Again, this may have enabled laser pulses towards the end of processing to penetrate the bulk with multiple pulses creating the holes observed.

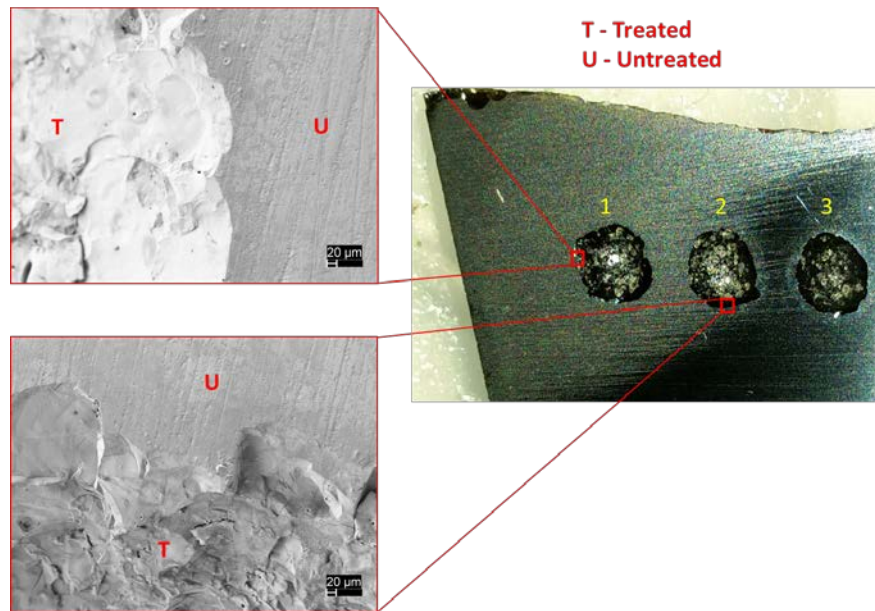


Figure 52. Secondary electron images showing effects of LDHP treatment on the surface of tektite (sample ID 21DEC15 Tektite). Image of border in area 1 showing treated and untreated sections (top left). Image of border in area 2 showing treated and untreated sections (bottom left).

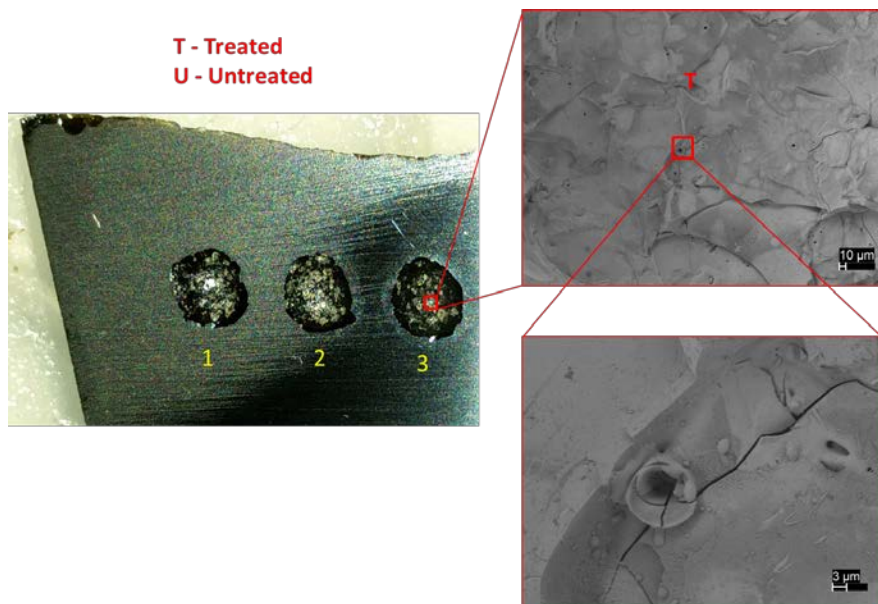


Figure 53. Secondary electron images showing effects of LDHP treatment on the surface of tektite. Treated surface in area 3 (top right). Increased magnification in the center of area 3 showing a hole in the surface and the appearance of material solidification after melting (bottom right).

EDS analysis was performed on the treated (six areas) and untreated (six areas) areas in and around each crater and averaged. Untreated areas were chosen to be as close to the rim of the craters (treated areas) as practically as possible. This analysis showed significant changes in chemical composition among the major oxides (Table 8). Based on a comparison of the untreated areas and the treated areas in each crater, an increase in SiO_2 , Fe_2O_3 , K_2O , CaO , and TiO_2 was observed, and a decrease in MgO and Na_2O . For Al_2O_3 , a decrease was observed in craters 1 and 2, but an increase in crater 3. To explain this, material inhomogeneity is not considered due to the vast differences when comparing this observation to chemical composition of the bulk tektite. It is possible particles created by spallation of the surface may be precipitating in and around the treated surface during LDHP.

Table 8. Comparison of chemical composition between bulk tektite sample, average of post-LDHP untreated areas, crater 1, crater 2 and crater 3.

<i>Oxide, Wt%</i>	<i>Bulk Tektite Wt%</i>	<i>Untreated Avg Composition Wt%</i>	<i>Crater 1 (100 pulses) Wt%</i>	<i>Crater 2 (100 pulses) Wt%</i>	<i>Crater 3 (200 pulses) Wt%</i>
<i>SiO_2</i>	72.54	66.76	75.04	74.82	87.58
<i>Al_2O_3</i>	12.31	15.64	13.65	13.66	16.54
<i>Fe_2O_3</i>	6.60	1.80	2.83	3.28	2.97
<i>K_2O</i>	2.52	0.30	1.63	1.62	1.80
<i>CaO</i>	2.03	0.20	1.27	1.34	1.60
<i>MgO</i>	2.36	4.69	3.28	3.32	3.72
<i>TiO_2</i>	0.89	0.11	0.43	0.44	0.55
<i>Na_2O</i>	0.75	4.95	1.87	1.52	1.91

b. Studies on Particles in Deionized Water after LDHP

Secondary electron images and SEM-EDS analysis of the suspended particles in deionized water showed oxide particles rich in Si between 100 nm and 2 μm in size, Ti-rich oxide particles ranging from 100–500 nm, Fe-rich oxide particles ranging from 50–250 nm, and Al-rich oxide particles 2–3 μm in size (Figure 54). Thus, it appears that there are two types of SiO_2 particles: (i) larger micron-sized particles with sharp edges and (ii) fine spheroidal particles as can be seen in the Si SEM-EDS image in Figure 54. Figure 55

shows three particles (as indicated by the red boxes) analyzed for chemical composition. In this particular sample, Table 9 and Figure 55 show the difference in chemical composition among the particles: oxide particle 1 being Al-rich with 61.19 wt% Al_2O_3 , oxide particle 2 being Al-rich with 90.37 wt%, and oxide particle 3 rich in Fe with 76.26 wt% Fe_2O_3 . This observation clearly showed the separation of transition element-rich particles from the bulk during LDHP. With many of the particles observed being in sub-micron size, it must be noted that the quantitative analysis must be carefully considered due to the large electron interaction volume and thus the matrix effects from the large tektite particle to which the inclusions are attached to. However, it is critical to note that EDS maps provide important clues towards the potential mechanism of LDHP by indicating that there are many particles rich in heavy elements such as Ti and Fe in the samples.

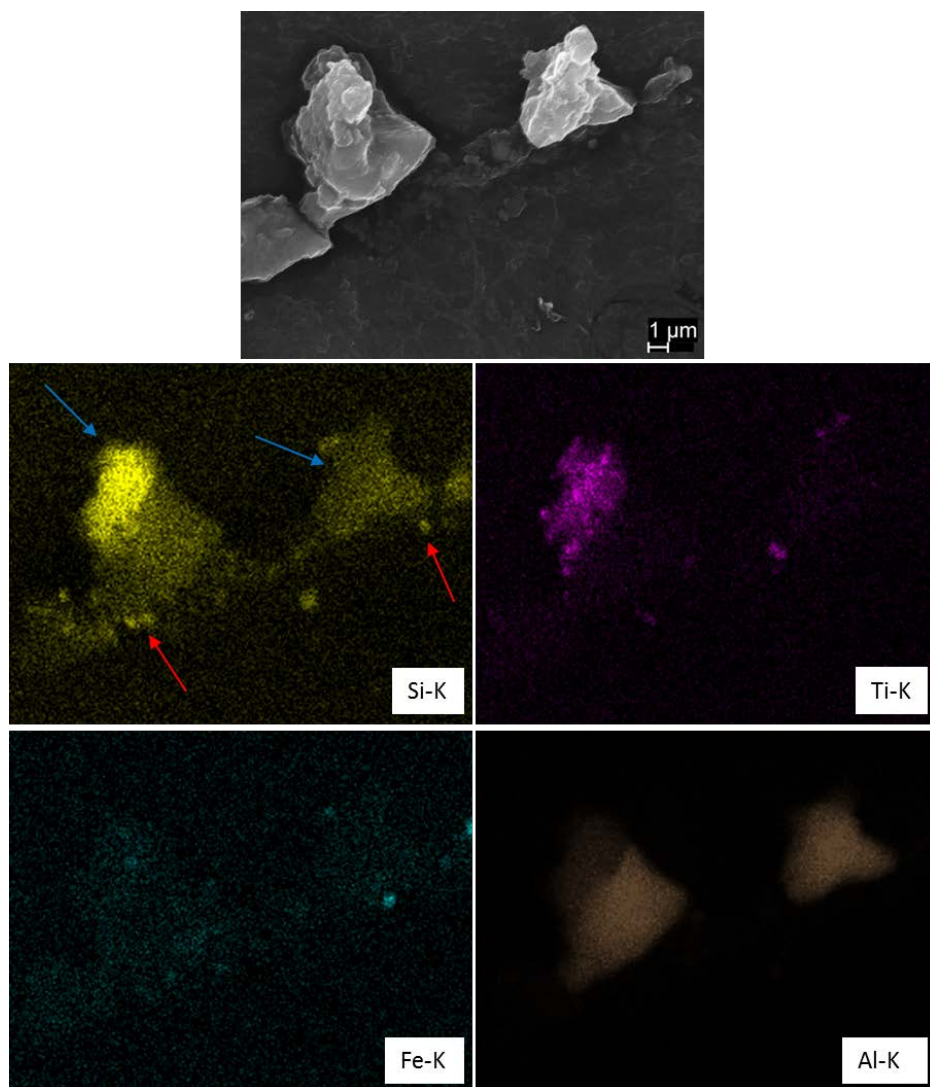


Figure 54. Secondary electron image of post-LDHP tektite particles collected from deionized water (top). SEM-EDS mapping showing Si-rich oxide particles (middle left), Ti-rich oxide particles (middle right), Fe-rich oxide particles (bottom left) and Al-rich oxide particles (bottom right).

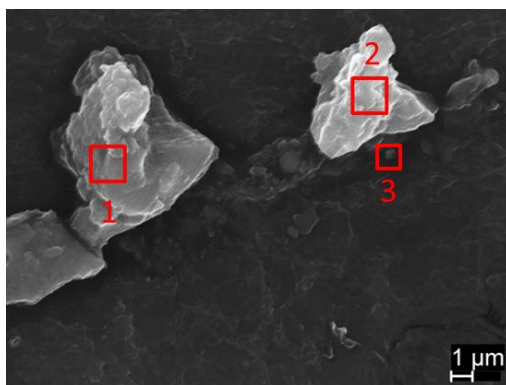


Figure 55. Secondary electron image of post-LDHP tektite particles analyzed showing significantly different chemical compositions. Red boxes indicate particles analyzed.

Table 9. Comparison of chemical composition between bulk tektite sample, post-LDHP particle 1, post-LDHP particle 2 and post-LDHP particle 3.

<i>Oxide, Wt%</i>	<i>Bulk Tektite Wt%</i>	<i>Post-LDHP Tektite Particle 1 Wt%</i>	<i>Post-LDHP Tektite Particle 2 Wt%</i>	<i>Post-LDHP Tektite Particle 3 Wt%</i>
<i>SiO₂</i>	72.54	23.78	8.25	6.26
<i>Al₂O₃</i>	12.31	61.19	90.37	12.76
<i>Fe₂O₃</i>	6.60	0.92	0.38	76.26
<i>K₂O</i>	2.52	0.11	0.10	0
<i>CaO</i>	2.03	0.52	0.03	0.25
<i>MgO</i>	2.36	0.10	0.24	2.17
<i>TiO₂</i>	0.89	11.63	0.05	0
<i>Na₂O</i>	0.75	1.75	0.59	2.30

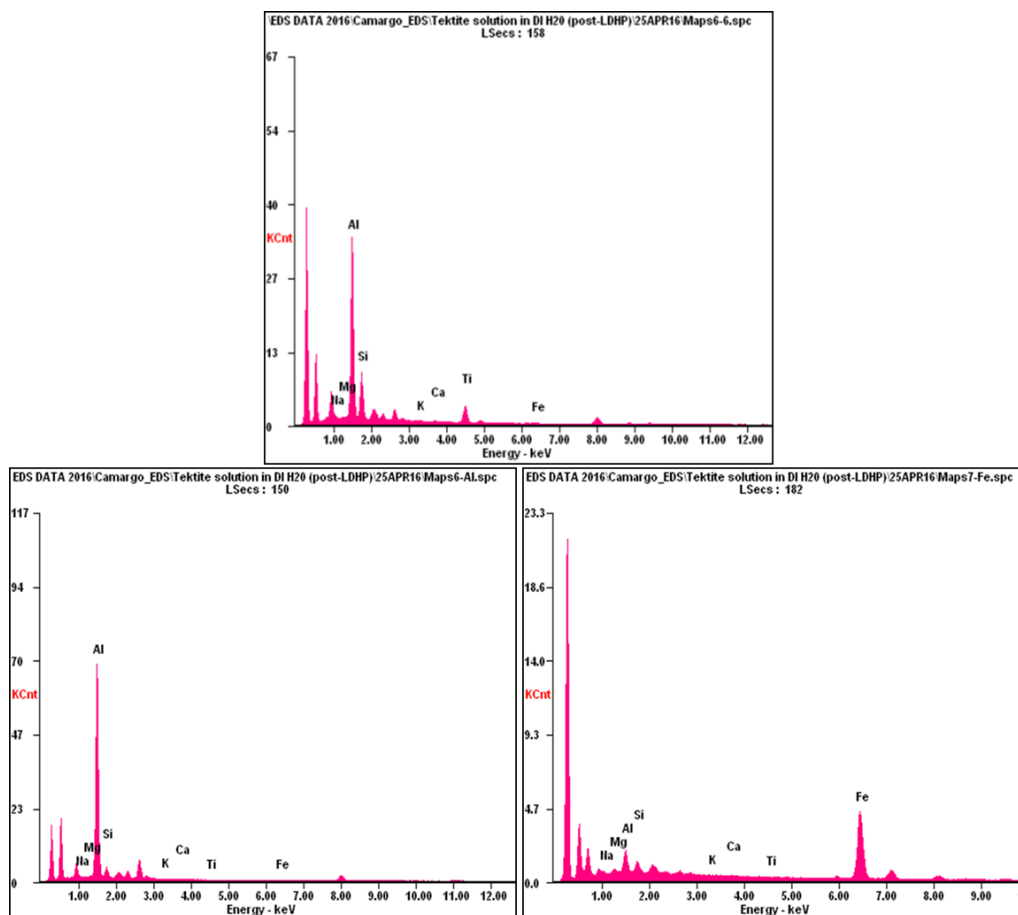


Figure 56. EDS spectra of particle 1 (top), particle 2 (bottom left) and particle 3 (bottom right) from post-LDHP tektite particle sample.

TEM analysis on the same sample of suspended particles in deionized water showed particles that appeared to contain heavy elements based on BF-STEM and HAADF-STEM images (Figure 57). Figure 58 shows STEM-EDS maps of particles rich in Si in the range of 100–250 nm, a Ti-rich oxide particle 150 nm in size, Fe-rich oxide particles in the range of 100–250 nm and an Al-rich particle 100 nm in size. In Figure 57, based on the EDS maps, particles labeled 1 may be pieces of bulk tektite since it is presumed these particles contain SiO_2 , Fe_2O_3 , and Al_2O_3 . Particle 2 is presumed to be SiO_2 , particle 3 is presumed to be TiO_2 , particles 4 are presumed to be Fe_2O_3 , and particle 5 is presumed to be Al_2O_3 . Some particles rich in Si were observed to have a polyhedral/angular morphology and were observed mostly as particles closer to 1 μm in size. Interestingly, one also observes many fine, spheroidal SiO_2 particles as well

identical to the observation in the earlier SEM-EDS maps. Ti-rich particles were observed in semi-spherical and polyhedral shapes usually in the 150–500 nm range. Fe-rich particles were also observed in a large size range, 50 nm – 1 μm , usually in a polyhedral shape, and observed in larger clusters. Particles rich in Al were observed in the 25 – 500 nm size range, in polyhedral shapes, and often in the upper end of the size range in larger clusters. Based on these observations, it appeared that the larger, sharp-edged Si-rich particles seen in these samples may be pieces of tektite removed from the bulk during LDHP. On the other hand, the smaller, spheroidal-shaped Si-rich particles may potentially be the combining of precipitate Si particles in the deionized water during LDHP.

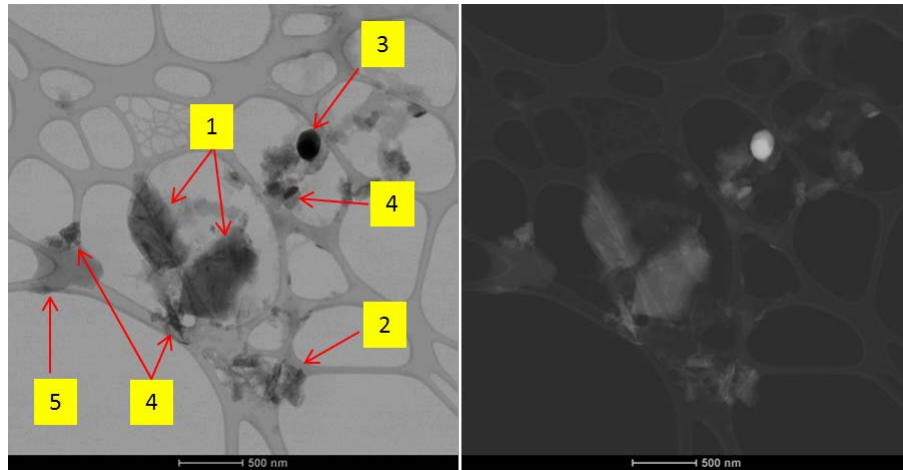


Figure 57. BF-STEM (left) and HAADF-STEM (right) images of crushed tektite particles. Scale bar 500 nm.

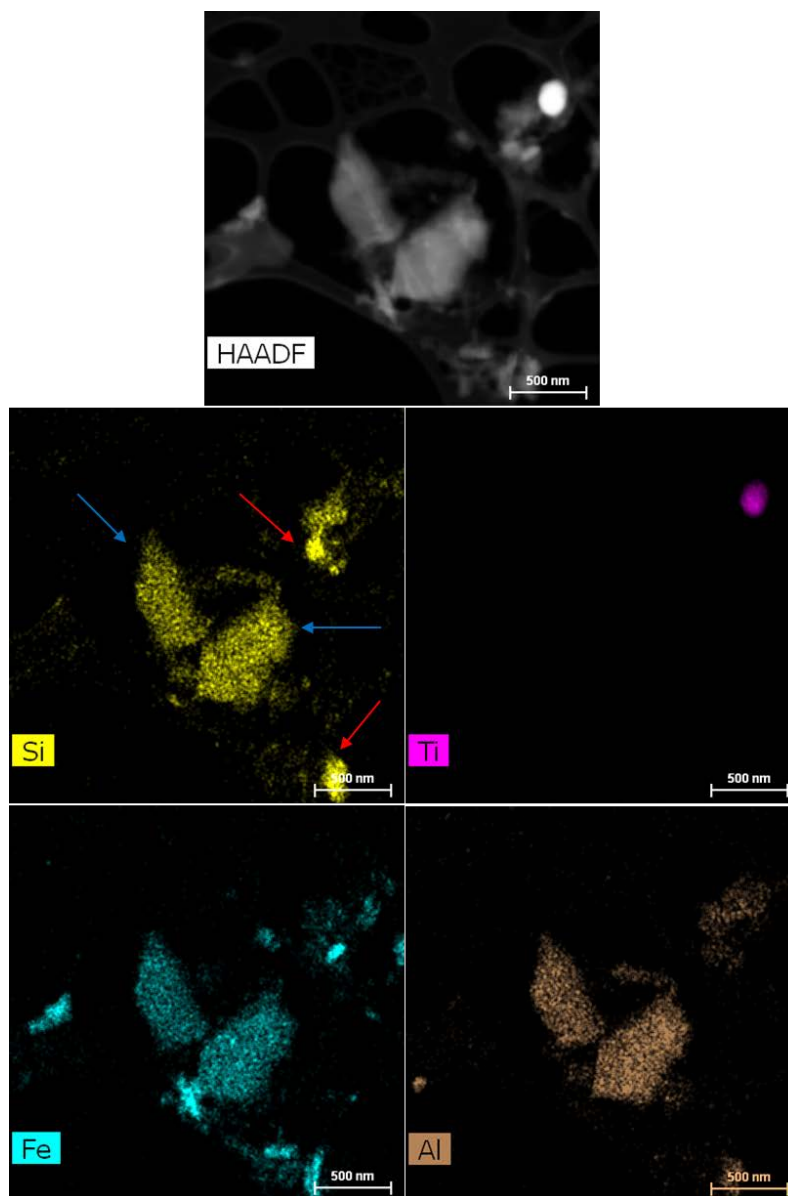


Figure 58. STEM-EDS mapping showing oxide particles rich in Si (middle left), Ti (middle right), Fe (bottom left) and Al (bottom right).

In summary, similar to bulk obsidian, the bulk tektite studied mostly consisted of the amorphous silica with smaller quantities of crystalline oxides. When crushed, a color change was also observed from black in its bulk for to light grey (in this case with a hint of yellow) again, suggesting the separation of inclusions from the bulk. SEM-EDS mapping of crushed tektite showed micron-sized oxide particles rich in Fe and Al in the

range of 1–4 μm . STEM-EDS mapping of the crushed tektite showed oxide particles rich in Si, Ti, and Al, between 50 nm – 2 μm , typically within larger SiO_2 particles.

After LDHP treatment, the bulk tektite sample showed the formation of three craters with larger crystals on the surface when compared to the bulk obsidian samples. Similarly, the cleavage-like appearance observed on the treated surface suggest spallation. Also observed, in the form of small holes, was the appearance of material solidification after melting indicating the generation of high-temperatures on the surface. The combination of translucent crystals and SEM-EDS chemical analysis of the untreated and treated surfaces suggests, again, removed material, possibly in ionic form, precipitating and redeposited onto the surface. SEM-EDS and STEM-EDS analysis of the suspended particles showed oxide particles rich in Si, Ti, Fe and Al ranging from 25 nm - 2 μm , while analysis of other oxide particles showed a similar chemical composition to bulk tektite. Morphology of these particles were mostly polyhedral for larger particles and spheroidal for smaller particles. The general observations made were fewer micron-sized SiO_2 particles with various oxides embedded within and a greater number of nm-sized oxide particles rich in transition metals. The observations made here further support the notion of the spallation effect of LDHP and the possible formation of precipitates.

C. SUMMARY OF POST-LDHP PARTICLES OBSERVED

Observation of the suspended particles (samples 21DEC15 Tektite and obsidian BC14SN) generated by LDHP, regardless of the laser conditions, showed a consistent pattern with regards to the type of oxide particle, size range, and morphology, with the difference being if particles were observed in clusters or not (Table 10). Sample BC14 of obsidian showed larger oxide particles, however, since this sample was collected from presumably heavier particles that accumulated on the bottom of the LDHP apparatus.

The relatively larger particles of the glass found in the deionized water sampled collected after LDHP may be the result of spallation by laser pulses impacting the material surface. The fine particles on the other hand are perhaps the result of complex ions of the elements released into the liquid media that cluster to form fine particles or precipitates. These precipitates once formed may certainly undergo subsequent oxidation

in the water. Overall, the observations made through the multiple characterization techniques suggests that transition elements are preferentially released into the liquid media by LDHP.

Table 10. Summary of post-LDHP particles observed.

<i>Particle Source</i>	<i>Laser Conditions</i>	<i>Oxide Particle</i>	<i>Size Range</i>	<i>Morphology</i>	<i>Comments</i>
Obsidian (sample ID: BC14)	1053-nm laser, 5 J/cm ² fluence, 17-ns pulse, 200 pulses	Si	1 - 25 µm	Polyhedral/angular	
		Ti	-	-	
		Fe	1 - 5 µm	Polyhedral/angular	
		Al	1 - 25 µm	Polyhedral/angular	
Obsidian (sample ID: BC14SN)	1053-nm laser, 5 J/cm ² fluence, 17-ns pulse, 200 pulses	Si	50 nm - 1 µm	Polyhedral/angular	Polyhedral/angular observed mostly as larger particles
		Ti	150 - 500 nm	spheroidal	Observed often in smaller clusters
		Fe	50 nm - 1 µm	spheroidal	Observed often in smaller clusters
		Al	25 - 500 nm	Polyhedral/angular	Observed as larger particles and in small clusters
Tektite (sample ID: 21DEC15 Tektite)	1065-nm laser, 2.6 J/pulse, ~40 J/cm ² fluence, 10-µs pulse, 100-200 pulses	Si	100 nm - 2 µm	Polyhedral/angular & spheroidal	Polyhedral/angular observed mostly as larger particles, spheroidal observed mostly as smaller particles
		Ti	100 - 500 nm	Spheroidal	Typically observed as isolated particles
		Fe	50 nm - 1 µm	Polyhedral	Observed often in larger clusters
		Al	25 - 500 nm	Polyhedral	Observed often in larger clusters

To compare, the crushed samples were observed to contain greater instances of larger micron-sized particles with compositions similar to that of the bulk material. Additionally, much fewer instances of transition element-rich oxides were observed in both crushed obsidian and tektite samples.

Figure 58 is provided to illustrate a preliminary idea for a possible mechanism of LDHP: (1) Laser impacts bulk material at designated laser parameters, (2) impact of laser forms crater at material surface creating a cloud of suspended particles and causing heavier particles to settle and collect below the material holding apparatus, and (3) suspended particles are a result of two events, (i) complex ions released into liquid media that combine to form fine particles/precipitates and (ii) spallation by laser pulses

impacting the surface of the material. Further investigation is needed through future studies towards understanding the mechanism of LDHP and the creation of particles.

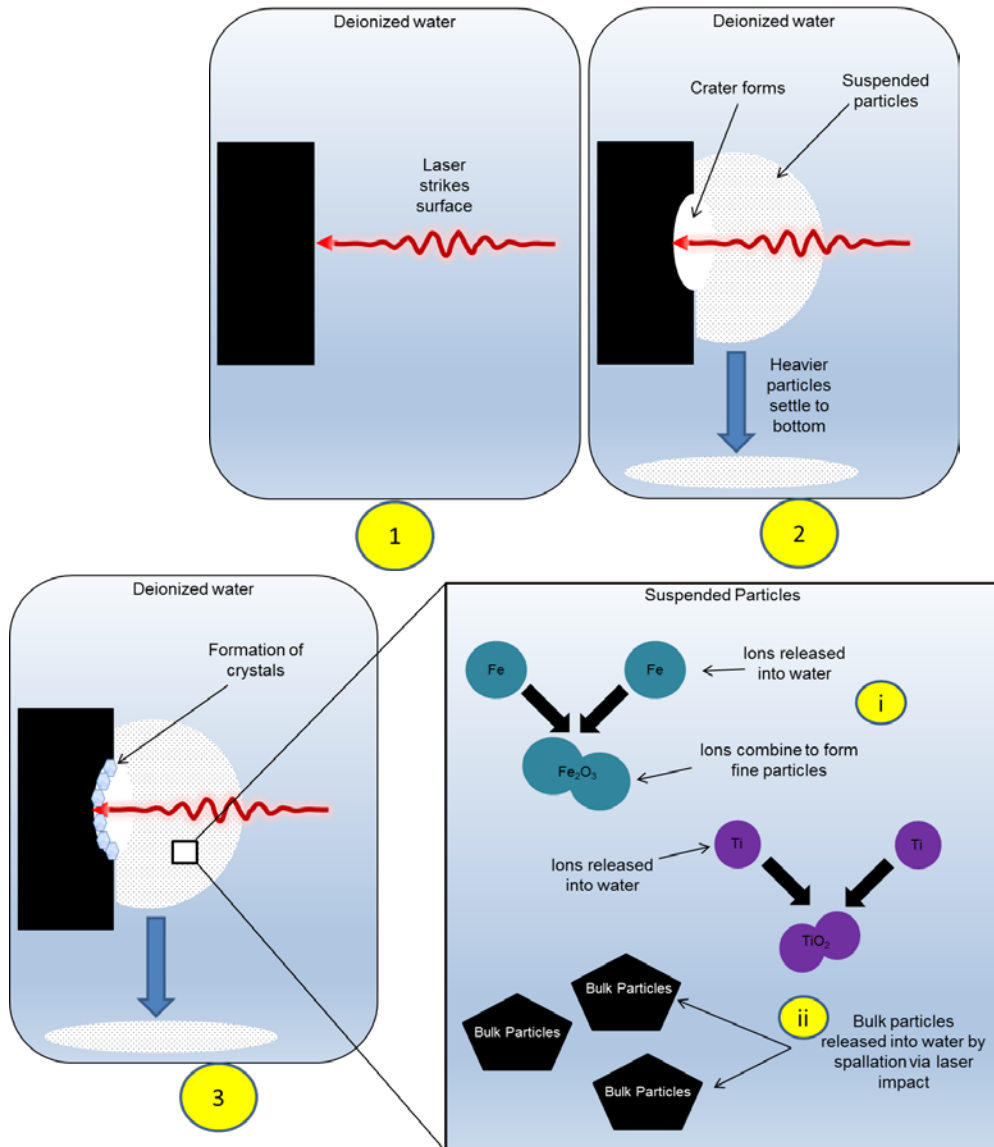


Figure 59. Diagram of possible mechanism of LDHP.

THIS PAGE INTENTIONALLY LEFT BLANK

IV. CONCLUSION

This study showed LDHP created nano- and micron-sized particles from two naturally occurring materials, obsidian and tektite. Multiple characterization techniques were used to determine the morphology, microstructure, and chemical composition of the base material, products of LDHP and its effects on the material surface.

XRD data showed the bulk obsidian studied as mostly amorphous with some crystallinity. SEM-EDS analysis showed that bulk obsidian is a relatively heterogeneous material composed mostly of SiO_2 with smaller quantities of oxides making up the rest of its chemical composition in some variation. When crushed, a color change was observed from black in its bulk form to light grey, suggesting separation of inclusions from its glassy matrix. SEM-EDS mapping of obsidian in bulk and crushed form showed micron-sized oxide particles rich in Fe and Al as small as 2 μm and as large as 20 μm . STEM-EDS mapping of the crushed obsidian showed nm-sized oxide particles rich in Si, Ti, Fe, and Al, between 40–800 nm, typically within larger SiO_2 particles.

After LDHP treatment, each bulk obsidian sample showed the formation of craters. One bulk sample contained a few small areas of the surface that appeared optically white/translucent while another bulk sample showed the entire surface as optically white/translucent. SEM analysis of these craters showed evidence of spallation from the cleavage-like appearance of the surface material removed to form each crater. Also observed was the appearance of material solidification after melting indicating the generation of high-temperatures on the surface assumed to be the result of repeated impact of pulses during laser processing. The larger/heavier particles collected after LDHP also appeared optically white/translucent. SEM-EDS chemical analysis and mapping showed oxide particles rich in Si and Fe, while analysis of other oxide particles showed a similar chemical composition to bulk obsidian. Similarly, STEM-EDS mapping of the suspended particles showed greater quantities of what are presumed to be oxide particles rich in Si, Fe, Ti, and Al. Generally, post-LDHP obsidian particles showed a varying range of particle sizes and morphology: (i) heavier particles collected from the bottom of the LDHP apparatus were observed to be between 1–25 μm with sharp,

polyhedral shapes and (ii) suspended particles were observed to be between 25 nm and 1 μm in spheroidal and polyhedral shapes. Overall, two general observations were made based on these results: (i) fewer micron-sized SiO_2 particles with various oxides embedded within and (ii) greater number of nm-sized oxide particles rich in Fe, Ti, and Al.

Similar to the bulk obsidian, XRD data showed the bulk tektite studied as mostly amorphous with a varying degree of crystallinity. SEM-EDS analysis also showed that bulk tektite is a heterogeneous material composed mostly of SiO_2 with smaller quantities of oxides making up the rest of its chemical composition in some variation. When crushed, a color change was also observed from black in its bulk form to light grey (in this case with a hint of yellow) again, suggesting the separation of inclusions from the bulk. SEM-EDS mapping of crushed tektite showed micron-sized oxide particles rich in Fe and Al in the range of 1–4 μm . STEM-EDS mapping of the crushed tektite showed oxide particles rich in Si, Ti, and Al, between 50 nm – 2 μm , typically within larger SiO_2 particles.

After LDHP treatment, the bulk tektite sample showed the formation of craters. In this case, all three craters contained larger crystals on the surface when compared to the bulk obsidian samples. Similarly, SEM analysis of these craters showed evidence of spallation from the cleavage-like appearance of the surface material. Also observed, in the form of small holes, was the appearance of material solidification after melting indicating the generation of high-temperatures on the surface. Formation of the translucent crystals on the treated surface and SEM-EDS chemical analysis of the untreated and treated surfaces suggests, again, removed material, possibly in ionic form, precipitating and redeposited onto the surface. SEM-EDS analysis and mapping of the suspended particles showed oxide particles rich in Si, Ti, Fe and Si ranging from 50 nm - 2 μm , while analysis of other oxide particles showed a similar chemical composition to bulk obsidian. STEM-EDS mapping of the suspended particles showed greater quantities of what are presumed to be oxide particles rich in Si, Fe, Ti, and Al between 25 – 250 nm. Morphology of these particles were also observed to be mostly polyhedral for larger particles and spheroidal for smaller particles. Again, the general observations made were

fewer micron-sized SiO_2 particles with various oxides embedded within and a greater number of nm-sized oxide particles rich in transition metals.

Evidence suggests LDHP may create particles in two ways: (i) larger particles by way of spallation from laser pulses impacting the material surface and (ii) complex ions of the elements released into the liquid media that cluster to form fine particles or precipitates.

THIS PAGE INTENTIONALLY LEFT BLANK

V. FUTURE WORK

The findings in this study look promising in determining the mechanism of LDHP in the formation of particles. More work is certainly needed in observing the effects on LDHP on other types of materials, including a more in depth study on how the different laser parameters effects the formation of particles and the formation of craters on the material surface.

The use of surrogate materials will greatly help in validating procedures and simplify characterization. The materials in this study were shown to be relatively inhomogeneous based on analysis of different sections of the same sample. Homogenous materials can ensure chemical consistency throughout its composition, which will help directly associate observations made before and after LDHP with testing methods used.

This study only observed particles derived from LDHP in deionized water. Analysis of particles in other solutions may also help determine how fine particles are formed. Additionally, this study will require advanced methods in particle size analysis and further research in this area may potentially correlate the size of the particles with the laser parameters and type of material processed.

XRD analysis was not performed on the collected post-LDHP particles due to insufficient quantity. With enough particles, characterization with XRD will determine crystalline phases present including crystallite size analysis. Electron energy loss spectroscopy (EELS) is another technique that can provide quantitative analysis of low atomic number elements including their chemical bonding states in samples with multi-element oxides [23].

THIS PAGE INTENTIONALLY LEFT BLANK

LIST OF REFERENCES

- [1] *Nuclear Forensics Support*, IAEA Nuclear Security Series No. 2, International Atomic Energy Agency, Vienna, Austria, 2006, pp 1–3.
- [2] “Nuclear Forensics: Role, State of the Art, Program Needs,” Joint Working Group of the American Physical Society and the American Association for the Advancement of Science, Washinton DC, 2008.
- [3] N. Sharp et al., “Rapid analysis of trinitie with nuclear forensic applications for post-detonation material analyses,” *J. of Radioanalytical and Nucl. Chemistry*, vol. 302, no. 1, pp. 57–67, Oct. 2014.
- [4] R. P. Mariella Jr et al., “Laser comminution of submerged samples,” *J. of Appl. Physics*, vol. 114, no. 1, May 2013.
- [5] S. K. Menon et al., Characterization of Particles formed via Laser-Driven Hydrothermal Processing, unpublished.
- [6] R. P. Mariella Jr and Y. M. Dardenne, “Nuclear Radiation Cleanup and Uranium Prospecting,” U.S. Patent 9 250 353 B2, Feb. 2, 2016.
- [7] R. P. Mariella Jr et al., “Laser-Driven Hydrothermal Processing,” International Patent Application PCT/US2014/011120, Jan. 10, 2014.
- [8] R. P. Mariella Jr, private communication, May 2016.
- [9] G. N. Eby et al., “Trinitite redux: Mineralogy and petrology,” *Amer. Minerologist*, vol. 100, no. 2–3, pp. 427–441, Feb. 2015.
- [10] J. E. Ericson et al., “Chemical and physical properties of obsidian: A naturally occuring glass,” *J. of Non-Crystalline Solids*, vol. 17, no. 1, pp. 129–142, Jan. 1975.
- [11] J. A. O’Keefe, “Natural glass,” *J. of Non-Crystalline Solids*, vol. 67, no. 1, pp. 1–17, Sep. 1984.
- [12] G. H. R. Von Koenigswald, “The Problem of Tektites,” *Space Sci. Rev.*, vol. 3, no. 3, pp. 433–446, Oct. 1964.
- [13] J. Miller. Obsidian is hot stuff [Online]. Available:

<http://volcano.oregonstate.edu/book/export/html/205>

- [14] C. Ma et al., “The Origin of Color in “Fire” Obsidian,” *The Can. Mineralogist*, vol. 45, no. 1, pp. 551–557, Jun. 2007.
- [15] N. W. Bower, “Optimization of Precision and Accuracy in X-Ray Fluorescence Analysis of Silicate Rocks,” *Appl. Spectroscopy*, vol. 39, no. 4, pp. 697–703, Jul. 1985.
- [16] A. N. Thorpe and F. E. Senftle, “Submicroscopic spherules and color of tektites,” *Geochimica et Cosmochimica Acta*, vol. 28, no. 6, pp. 981–994, Jun. 1964.
- [17] C. Koeberl, “Tektite origin by hypervelocity asteroidal or cometary impact: Target rocks, source craters, and mechanisms,” Geological Society of America, Inc., Boulder, CO, Special Paper 293, 1992.
- [18] R. Akhter, N. Shirai and M. Ebihara, “Chemical characteristics of dalat tektites,” in *45th Lunar and Planetary Science Conference*, Houston, TX, 2014.
- [19] D. R. Chapman, “Australasian Tektite Geographic Pattern, Crater and Ray of Origin, and Theory of Tektite Events,” *J. of Geophysical Res.*, vol. 76, no. 26, pp. 6309–6338, Sep. 1971.
- [20] R. P. Mariella Jr, private communication, Apr. 2016.
- [21] R. P. Mariella Jr, private communication, Oct. 2015.
- [22] R. P. Mariella Jr, private communication, Dec. 2015.
- [23] S. K. Menon, Statement of Work: Characterization of Particles formed via Laser-Driven Hydrothermal Processing, unpublished.

INITIAL DISTRIBUTION LIST

1. Defense Technical Information Center
Ft. Belvoir, Virginia
2. Dudley Knox Library
Naval Postgraduate School
Monterey, California